



**UNIVERSIDAD AUTÓNOMA DE
SAN LUIS POTOSÍ**

FACULTAD DE MEDICINA



**CENTRO DE INVESTIGACIÓN EN CIENCIAS DE LA
SALUD Y BIOMEDICINA (CICSaB)**



**CARACTERIZACIÓN ULTRAESTRUCTURAL DE LA INFECCIÓN IN
VITRO DEL VIRUS SINCICIAL RESPIRATORIO.**

TESIS QUE PRESENTA

M.C. IGNACIO LARA HERNÁNDEZ

**PARA OBTENER EL GRADO DE
DOCTOR EN CIENCIAS BIOMÉDICAS BÁSICAS**

CO-DIRECTORES DE TESIS

**DR. MAURICIO COMAS GARCÍA
DR. ANDREU COMAS GARCÍA**

AGOSTO 2023

CRÉDITOS INSTITUCIONALES

Este trabajo se llevó a cabo bajo la tutoría del Dr. Andreu Comas García y del Dr. Mauricio Comas García en el Departamento de Microbiología de la Facultad de Medicina y en la Sección de Microscopia de Alta Resolución del Centro de Investigación en Ciencias de la Salud y Biomedicina (CICSaB), de la Universidad Autónoma de San Luis Potosí, con la beca otorgada por el CONACYT con número (CVU) 775699.

Tesis que presenta:

M.C. IGNACIO LARA HERNÁNDEZ

PARA OBTENER EL GRADO DE DOCTOR
EN CIENCIAS BIOMÉDICAS BÁSICAS

CODIRECTORES DE TESIS

DR. ANDREU COMAS GARCÍA

DR. MAURICIO COMAS GARCÍA

ASESORES INTERNOS

DRA. SOFÍA BERNAL SILVA.

DR. DANIEL ERNESTO NOYOLA CHERPITEL.

ASESOR EXTERNO

DRA. ROSA MARIA WONG CHEW.

JURADO

PRESIDENTE DE SINODALES:

DRA. PERLA DEL CARMEN NIÑO MORENO

SECRETARIA DE SINODALES:

DRA. SOFÍA BERNAL SILVA

SINODALES:

DR. DANIEL ERNESTO NOYOLA CHERPITEL

DRA. ROSA MARÍA WONG CHEW

AGOSTO 2023



Caracterización ultraestructural de la infección in vitro del virus sincicial respiratorio. Por Ignacio Lara Hernández. Se distribuye bajo una [Licencia Creative Commons Reconocimiento-NoComercial-CompartirIgual 4.0 Internacional](https://creativecommons.org/licenses/by-nc-sa/4.0/).

Ultrastructural and Functional Characterization of Mitochondrial Dynamics Induced by Human Respiratory Syncytial Virus Infection in HEp-2 Cells

Ignacio Lara-Hernandez ¹, Juan Carlos Muñoz-Escalante^{2,3}, Sofía Bernal-Silva ^{3,4}, Daniel E. Noyola ^{2,3}, Rosa María Wong-Chew ⁵, Andreu Comas-García ^{3,*} and Mauricio Comas-García ^{1,6,7,*}

¹ High-Resolution Microscopy Section, Center for Research in Health Sciences and Biomedicine, Autonomous University of San Luis Potosí, San Luis Potosí, 78210, Mexico; lara.ignacioh@gmail.com

² Center for Research in Health Sciences and Biomedicine, Autonomous University of San Luis Potosí, San Luis Potosí, 78210, Mexico; carlos.escalante@uaslp.mx (M.-E.J.C.); dnoyola@uaslp.mx (N.D.E.)

³ Department of Microbiology, School of Medicine, Autonomous University of San Luis Potosí, San Luis Potosí, 78210, Mexico; sofia.bernal@uaslp.mx

⁴ Genomic Medicine Section, Center for Research in Health Sciences and Biomedicine, Autonomous University of San Luis Potosí, San Luis Potosí, 78210, Mexico

⁵ Research Division, School of Medicine, National Autonomous University of Mexico, Mexico City, 04360, Mexico; rmwongch@yahoo.com.mx

⁶ Science Department, Autonomous University of San Luis Potosí, San Luis Potosí, Mexico

⁷ Molecular and Translation Medicine Section, Center for Research in Health Sciences and Biomedicine, Autonomous University of San Luis Potosí, San Luis Potosí, 78210, Mexico

* Correspondence: andreu.comas@uaslp.mx (C.-G.A.); mauricio.comas@uaslp.mx (C.-G.M.)

Abstract: Human respiratory syncytial virus (hRSV) is the leading cause of acute lower respiratory tract infections in children under five years of age and older adults worldwide. During hRSV infection, host cells undergo changes in endomembrane organelles, including mitochondria. This organelle is responsible for energy production in the cell and plays an important role in the antiviral response. The present study focuses on characterizing the ultrastructural and functional changes during hRSV infection using thin-section transmission electron microscopy and RT-qPCR. Here we report that hRSV infection alters mitochondrial morphodynamics by regulating the expression of key genes in the antiviral response process, such as Mfn1, VDAC2, and PINK1. Our results suggest that hRSV alters mitochondrial morphology during infection, producing a mitochondrial phenotype with shortened cristae, swollen matrix, and damaged membrane. We also observed that hRSV infection modulates the expression of the aforementioned genes, possibly as an evasion mechanism in the face of cellular antiviral response. Taken together, these results advance our knowledge of the ultrastructural alterations associated with hRSV infection and might guide future therapeutic efforts to develop effective antiviral drugs for hRSV treatment.

Keywords: human respiratory syncytial virus; mitochondrial alterations; ultrastructural characterization

1. Introduction

The human respiratory syncytial virus (hRSV), also known as human Orthopneumovirus, is an enveloped, single-stranded negative-sense RNA virus that encodes for 11 proteins. This virus belongs to the genus Orthopneumovirus and Pneumoviridae family [1].

Since it was discovered hRSV has been considered the main etiological agent of acute lower respiratory tract infections in children under the age of five and an important cause of pneumonia in elderly adults worldwide. In 2019, it was estimated that there were 33.0 million acute lower respiratory tract infections related to hRSV infections globally in children 0 to 60 months of age, of which 6.6 million were reported in infants < 6 months [2].

This virus is classified based on its antigenic reactivity to monoclonal antibodies directed against the viral attachment protein (G), and it is further divided into two subgroups: A and B [3]. The hRSV virion consists of viral envelope which has three viral transmembrane proteins: attachment (G), fusion (F), and the small hydrophobic (SH). The inner part of the virion contains the matrix (M) protein which surrounds the nucleoprotein complex. This complex consists of a 15 kb-long genomic RNA, the nucleoprotein (N), the phosphoprotein (P), the large polymerase subunit (L), and the M2-1/2 proteins [4].

Glycoprotein G is of particular interest because it has a larger variability with respect to the other hRSV proteins [5]. Based on this variability, new genotypes have been identified; in particular, duplications of the G protein's C-terminal domain have resulted in highly dominating genotypes. The first duplication found in hRSV-B was reported in 2003 and consisted of 60 nucleotides (nts) of the C-terminal (genotype BA), but it was determined that the duplication occurred near 1996 [6,7]. In 2012 a second duplication (72 nts) in this gene was reported on an hRSV subgroup A (genotype ON1) [8]. Later it was published that this duplication emerged in multiple locations around the world since 2009 [9] Since their identification, both the BA and ON1 genotypes have become the dominant genotypes worldwide [10]. However, it is not clear why genotypes with these duplications have resulted in replacement of all other variants.

The infectious viral cycle results in remarkable alterations of the cellular architecture. For example, certain viruses have shown to cause structural, functional, or biochemical alterations in cells to facilitate viral replication, virion assembly, and egress. In particular, the endomembranes can undergo dramatic changes because of the strategy of the viruses to hijack cell structures [11–13]. hRSV replication and transcription process occur in the cytoplasm and Golgi, but not in the nucleus [14–16]. Nonetheless, some viral proteins are imported into the nucleus. For example, the M2-1 viral protein promotes nuclei NF- κ B activation and Rel-A [17], and the M protein interacts with zinc finger protein 2, SMAD3, and chromatin, inhibiting the host cell transcription [18,19]. NS1 and NS2 inhibit IRF-3, inhibit INF activation, and induce STAT2 degradation [20,21]. Furthermore, it has been reported that hRSV antagonizes the innate

immune response mediated by MDA5 and MAVS [22,23]. Both proteins are part of the mitochondrial antiviral signaling system. In fact, hRSV interacts with the mitochondrial interface. This interaction impaired mitochondrial respiration by causing loss of mitochondrial membrane potential and increasing mitochondrial ROS [24]. The ultrastructural changes of the mitochondria, as a response to a viral infection, is probably one of the most studied examples of virus-induced organelle remodeling [25]. Yet we still do not fully understand how mitochondrial alterations contribute to viral replication and pathogenesis. Some viruses disrupt the mechanisms of mitochondrial dynamics to inhibit antiviral signaling. For example, hepatitis C virus enhances mitochondrial fission through the activation of Drp1, which is a protein associated with fission. Also, it inhibits innate immune responses and apoptosis by enhancing mitophagy [26]. Hepatitis B virus also inhibits the innate immune response and apoptosis by enhancing mitochondrial fragmentation and mitophagy through phosphorylation of Drp1 and upregulation of mitophagy-associated proteins Parkin and PINK1, which are ubiquitin kinases related with mitochondrial health [27]. In contrast, the measles virus (MeV) induces mitophagy to reduce the mitochondrial antiviral signaling protein levels and block the innate immune response [28].

The effect of hRSV infection on the mitochondria is not well understood. However, proteomic studies on hRSV-infected cells have identified changes in protein levels of several nuclear-encoded mitochondrial proteins such as voltage-gated anion channel (VDAC) protein and prohibitin (PHB). These proteins play a critical role regulating mitochondrial structure, function, and biogenesis [29,30]. Furthermore, it was found that hRSV infection hijacks the mitochondria during replication by redistributing them to the perinuclear region. This spatial redistribution is a microtubule/dynein-dependent process that is induced by the viral infection and results in changes in mitochondrial membrane polarization. These changes decrease the mitochondrial membrane potential and increase the levels of reactive oxygen species levels [31]. Nonetheless, little is known about hRSV-induced alterations in mitochondrial dynamics.

In this study, we explored the ultrastructural and functional changes of the mitochondria of HEp-2 cells infected with hRSV-A ON1. We found that hRSV infection induces alterations in mitochondria size (area) and Feret's diameter. Mitochondria of infected cells have an aberrant morphology: there is damage to the cristae, and there is a loss in the membrane integrity. We found that during early infection time points, hRSV infection promotes mitochondrial fusion associated with mitofusins (Mfn1) mRNA downregulation. Furthermore, except for transient overexpression at 24 h.p.i., we also found down-regulation of VDAC2. Surprisingly, the mRNA for the kinase-mediated mitophagy (PTEN-induced serine/threonine kinase, PINK1) mRNA was also suppressed during infection. Our results suggest that hRSV infection induces changes in mitochondrial dynamics that regulate activities linked to the fusion processes and the antiviral signaling pathways in mitochondria and inhibits mitophagy. Overall, these changes in

mitochondrial dynamics might imply a mechanism that contributes to the pathogenesis of RSV that could be essential to allow the formation of syncytia.

2. Materials and Methods

2.1. Cell Line Culture, Viral Stock and Treatments

HEp-2 cells (ATCC, CCL-23) were grown, following previous protocols for hRSV infections, in 6-well culture plates in 5% CO₂ and 37 °C in DMEM (ThermoFisher, Grand Island, NY, USA) supplemented with 5% fetal bovine serum (Gibco, Grand Island, NY, USA) and 1% streptomycin (Pisa, Guadalajara, Mexico) and penicillin (PiSA, Guadalajara, Mexico) [32–37].

The viral stock was generated from a clinical sample positive for hRSV, the genotype was assigned by sequencing the ectodomain region of the G gene and the isolated was used subsequently to infect confluent monolayer HEp-2 cells. The presence of the cytopathic effect of the virus was identified (by light microscopy after five days, and the presence of the virus was confirmed by qRT-PCR (with absolute quantification of the number of viral copies); a subculture was performed at MOI 5, and virus concentration was carried out at low speed starting from 25.2 x10⁶ infected cells at MOI 5 based on the protocol of Rayaprolu et al. [38]. The viral stock was quantified by qRT-PCR using the primers in Table 1 and stored for less than six months refrigerated at 4 °C.

Upon reaching 95% confluence, culture media was replaced by 1x PBS, and the cells were inoculated with a viral stock of hRSV NA1-ON1 genotype at a multiplicity of infection (MOI) of 10 and incubated for two hours with constant agitation every 15 min. After the absorption time, the inoculum was removed, and culture media supplemented with 1% fetal bovine serum was added and cultures were incubated at 37 °C with 5% CO₂. Infected cells were incubated for 2, 24, 48, 72, and 96 h; afterward, cells were washed with 1x PBS and fixed with 2% glutaraldehyde and 0.05% picric acid in 0.1-M cacodylate buffer pH 7.4 for 1 h at room temperature and then stored at 4 °C until processing for transmission electron microscopy (TEM). Cultures used for RT-qPCR were processed under the same conditions up until harvesting; at that point, they were incubated for 10 min with 500 µL of trypsin (TrypLE Express, Grand Island, NY, USA), and 1 mL of supernatant was taken from cultures corresponding to each condition to detach the cells. The sample was homogenized and placed and maintained at 4 °C until RNA extraction.

2.2. Transmission Electron Microscopy

Thin-section TEM was used to characterize the ultrastructural modifications of infected cells. Cultures were processed using the previously described methodology [39]. Briefly, after the samples were fixed as described in the previous section, these were washed three times with 0.1 M sodium cacodylate buffer pH 7.2; the samples were further fixed with 1% osmium

tetroxide in 0.1 M sodium cacodylate for one hour at room temperature in the dark. The cultures were rinsed twice with the sodium cacodylate buffer and once with 0.1 sodium acetate buffer pH 4.5, block-stained with 0.5% uranyl acetate in 0.1 M sodium acetate for one hour at room temperature in the dark. Subsequently, the cells were washed three times with the 0.1 M sodium acetate and two times with MilliQ water before being left to incubate in MilliQ water overnight. The following day, cells were dehydrated with ethanol with increasing concentration (35%, 50%, 70%, 95%, and 100%) for 10 min and three times for each concentration, then cells were rinsed three times with Embed 812 resin (Electron Microscopy Science, Hatfield, PA, USA). Finally, the cells were embedded in the EMBed 812 resin and polymerized for 48 h at 55 °C. Ultrathin sections (70 nm) were obtained using an EM-UC7 ultramicrotome (Leica Inc., Karnataka, India) and transferred to 100-mesh copper grids and stained with 0.5% uranyl acetate and 0.5% lead citrate. After staining, the grids were kept in closed Petri dishes containing dry pellets of NaOH and silica. The samples were visualized in a JEM-JEOL-2100 transmission electron microscope at 200 kV using a Gatan 4K camera. The digital electron micrographs were recorded with the Digital Micrograph (Gatan Inc., Pleasanton, CA, USA) software and analyzed with ImageJ and Fiji (NIH, Bethesda, ML, USA). Each sample was done in duplicate.

2.3. Qualitative Morphological Evaluation

Micrographs were evaluated qualitatively using a method to correlate the degree of ultrastructural damage with its specified stage of mitochondrial injury using the previously described methodology [40,41]. This classification has four classes and are described in Table 2.

2.4. Morphometric Analysis

The morphometric analysis was performed using the Fiji software version 2.9.0/1.53 (NIH) by randomly selecting 25 micrographs per sample. The mitochondrial shape descriptors and size measurements were obtained by manually selecting the contours. The size descriptors studied were the surface area (or mitochondrial size); the perimeter, and the Feret's diameter (which is the largest distance between two points). The shape descriptors analyzed were the aspect ratio (AR) (major axis/minor axis) which represents the "length-to-width ratio"; the form factor (FF) ($\text{perimeter}^2/4\pi \times \text{Surface area}$) that reflects the complexity and branching appearance of mitochondria; the circularity ($4\pi \times \text{surface area}/\text{perimeter}^2$), and the roundness ($4 \times \text{surface area}/\pi \times \text{major axis}^2$). These last two parameters are two-dimensional indices of sphericity with values of 1 denoting perfect spheroids. Once the data was obtained, the calculated values were imported into Microsoft Excel and Prism 9 (GraphPad Software, San Diego, CA, USA) for data analysis.

2.5. RNA Extraction

Viral RNA was extracted from the cell cultures at different times post-infection (2-, 24, 48-, 72- and 96-h post-infection) using the QIAamp® Viral RNA extraction kit (Qiagen Brand 52906, Germantown, MD, USA) and was eluted in the AVE buffer (RNAse-free water containing 0.04% sodium azide). Total RNA concentration and purity was determined using a spectrophotometer nanodrop. Only samples with an OD_{260nm}/OD_{280nm} between 1.8 and 2.0 were further processed. Samples were stored at -80 °C until use.

2.6. Analysis of Gene Expression by Reverse Transcription Polymerase Chain Reaction (RT-qPCR)

Quantitative RT-PCR was performed using the Luna® Universal One-Step RT-qPCR kit (New England BioLabs, Ipswich, MA, USA) in a Mic qPCR Cyclor (Bio Molecular Systems) magnetic induction thermocycler, using the glyceraldehyde-3-phosphate dehydrogenase (GAPDH) gene as an endogenous gene. Primers used to quantify expressions of mRNAs related to the mitophagy process PINK1 (NM_032409.3), VDAC2 (NM_003375.5), and Mfn1 (NM_033540.3) mRNA expression are shown in Table 2. The reaction (10 µL total volume) contained 5 µL Luna Universal One-Step Reaction Mix (2×) (New England BioLabs), 2 µL RNA (10 ng/mL), 2.1 µL nuclease-free water, 0.4 µL of forward and reverse primers each at a concentration of 10 µmol/L, and 0.5 µL of Luna WarmStart® RT Enzyme Mix (20×) (New England BioLabs, Ipswich, MA, USA). The reaction process consisted of a retrotranscription of 55 °C for 10 min and 95 °C for 1 s, followed by 40 cycles of 95 °C for 10 s and 60 °C for 30 s, and finally, a dissociation curve from 60 °C to 95 °C with a 0.3% increase. Subsequently, the $2\Delta\Delta C_t$ between the target gene and the housekeeping GAPDH gene was calculated using the previously established method [42]. GAPDH was chosen as a housekeeping gene based on previous studies with hRSV [43,44]. Furthermore, the relative expression of this housekeeping gene in the infected cells with respect to the mock-infected cells was not statistically significantly different at any time point (Supplementary Figure S1). All experiments were performed in duplicate, and we analyzed two biological replicas.

2.7. hRSV Viral Copy Quantification by Reverse Transcription Polymerase Chain Reaction (RT-qPCR)

10 ng of RNA were used for the Retrotranscription using the RevertAid H kit Minus First Strand cDNA Synthesis Kit (Thermo Scientific, Waltham, MA, USA). First Strand cDNA Synthesis Kit (Thermo Scientific, Waltham, MA, USA). From this cDNA, PCR was performed for absolute quantification of RSV viral copies using the following primers: MCVF (5'-GGCAAATATGGAAACATACGTGAA-3') and MCVR (5'-TCTTTTTCTAGGAC

ATTGTAYTGAACA-3'), at a final concentration of 0.25 μ m, which are directed to the intergenic region between the RSV P and M genes and generate an 87 bp product. As a control for the standard curve, a 2752 bp pUCIDT that has a 500 bp synthetic construct including the quantification PCR target site was used. qPCR was performed with the Maxima SYBR Green/ROX qPCR Master Mix (2x) kit (Thermo Scientific, Waltham, MA, USA) as indicated in the insert, the cDNAs obtained were analyzed in duplicate, as well as the 6 points of the standard curve. The data of the experiment were considered adequate if the standard curve correlation coefficient was greater than 0.98. The quantification was carried out by means of the linear regression method using the parameters of the line from the standard curve. All experiments were performed in duplicate, and we analyzed two biological replicas.

2.8. Statistical Analysis

The statistical analysis was performed using GraphPad Prism 9 (GraphPad, San Diego, CA, USA). The data distribution for each of each data set was assessed using a Shapiro-Wilk as a test of normality to assess whether the data series conformed to a normal distribution. Nonparametric data were described as median (interquartile range). Comparisons within groups were made using the Friedman test. Comparisons between groups were made using the Mann–Whitney U test. For categorical variables we performed a 2 x 2 analysis and the Fisher's exact test. In all cases, $p < 0.05$ was considered statistically significant. The data in Figures that plot the Feret's diameter, area, and RT-qPCR, are shown as boxplot and the lines indicate the data between the lower quartile (25%) and the lower extreme, and between the upper quartile (75%) and the upper extreme.

3. Results

3.1. Effects of hRSV ON1 Genotype Infection on the Morphology of the Mitochondria of the HEP-2 Cell Line

The mitochondrial morphology of the control HEP-2 (mock-infected) and infected cells were characterized at the ultrastructural level by thin-section TEM. The morphology of the mitochondria in control HEP-2 cells remained consistent across all time points, with the classical shape, a double mitochondrial membrane, and defined cristae (Figure 1A–D). In contrast, we found significant changes in the mitochondrial ultrastructure of hRSV ON1infected cells. At 2-h post-infection (hpi) (Figure 1E), irregular or swirling mitochondrial cristae were seen, and at 24-hpi (Figure 1F), the mitochondria have swollen matrix, discontinuous outer membranes, and fragmented cristae. At 48-hpi (Figure 1G), the mitochondria had varied shapes and sizes, as well

as a discontinuous outer membrane and fragmented cristae. Finally, at 72-hpi (Figure 1H), the mitochondria have irregular or swirling cristae.

3.2. Morphological Characterization of Mitochondria Infected with RSV ON1 in the HEp-2 Cell Line

This organelle was classified into four classes to determine the degree of mitochondrial damage in HEp-2 cells. Class I (Figure 2A) corresponds to normal mitochondria with densely packed longitudinal cristae and an electron-dense matrix. Class II (Figure 2B) is characterized by bulging, irregular, or swirling cristae that have lost their orientation and/or narrowness. Class III (Figure 2C) presents varied shapes and sizes, with discontinuous mitochondrial membranes, fragmented cristae, swollen, and electro-lucent matrix. Finally, class IV (Figure 2D) refers to mitochondria with disrupted membranes, disrupted mitochondrial cristae, and diffuse appearance. Between 50 and 150 mitochondria were evaluated in each sample, and the degree of mitochondrial damage was observed to increase gradually over time.

We analyzed the ultrastructural changes at 2-hpi in the control group and 98.3% of the mitochondria exhibited normal morphology (Figure 2E) and only 1.7% exhibited an alteration in their morphology, particularly damage in the mitochondrial cristae (Figure 2F). In contrast, in the hRSV infected group, 52% of the mitochondria exhibited normal morphology (Figure 2E), 34.7% exhibited damage in the mitochondrial cristae (Figure 2F), and 13.3% showed damage to cristae and mitochondrial membrane (Figure 2G).

At 24-hpi, in the control group, 59.3% of the mitochondria exhibited normal morphology (Figure 2E), 20.3% exhibited damage in the mitochondrial cristae (Figure 2F), 17% showed damage to cristae and mitochondrial membrane (Figure 2G), and 3.4% of the mitochondria showed a disrupted morphology (Figure 2H). In the infected groups, 6.6% of the mitochondria exhibited normal morphology (Figure 2E), 50% exhibited damage to the mitochondrial cristae (Figure 2F), 38.5% showed damage to cristae and mitochondrial membrane (Figure 2G), and 4.9% exhibited a destroyed morphology (Figure 2H).

The control group at 48-hpi showed that 83.6% of the mitochondria exhibited normal morphology (Figure 2E), 7.3% exhibited damage to the mitochondria cristae (Figure 2F), and 9.1% showed damage to cristae and mitochondrial membrane (Figure 2G). In the infected cells, 2.4% of the mitochondria exhibited normal morphology (Figure 2E), 23.5% exhibited damage to the mitochondrial cristae (Figure 2F), 62.4% showed damage to cristae and mitochondrial membrane (Figure 2G), and 11.7% exhibited a destroyed morphology (Figure 2H).

At 72-hpi, in the control group, 32.7% of mitochondria had normal morphology (Figure 2E), 64.5% had damaged mitochondrial cristae (Figure 2F), and 2.8% exhibited damage in the cristae and the mitochondrial membrane (Figure 2G). In the infected cells, 7.7% of the mitochondria

exhibited normal morphology (Figure 2E), 52.6% exhibited damage to the mitochondrial cristae (Figure 2F), 38.5% showed damage to cristae and mitochondrial membrane (Figure 2G), and 1.2% showed morphological disruption (Figure 2H).

Finally, when the control group was analyzed at 96-hpi, 67.4% of the mitochondria had normal morphology (Figure 2E), 24.7% has damaged mitochondrial cristae (Figure 2F), and 7.9% showed damage to cristae and mitochondrial membrane (Figure 2G). In contrast, in the infected cells, 17.2% of the mitochondria exhibited normal morphology (Figure 2E), 50.3% exhibited damage to the mitochondrial cristae (Figure 2F), 23.6% showed damage to cristae and mitochondrial membrane (Figure 2G), and 8.9% exhibited a destroyed morphology (Figure 2H).

In the control group Fisher's exact test indicates that the prevalence of mitochondria in the mock infected cells with normal morphology (Class I) is higher compared to abnormal morphology of mitochondria at any time point (Classes II, III, and IV) ($p < 0.0001$). Furthermore, the same test indicated that the infected cells have a higher number of mitochondria with abnormal morphology (Classes II, III, and IV) than the mock infected cells ($p < 0.0001$).

These results show that the hRSV-ON1 infection alters the structure of the mitochondria; specifically, the morphology of mitochondrial cristae and the integrity of mitochondrial membranes are greatly affected by the infection. These results suggest that hRSV-ON1 infection is related to alterations in the function of mitochondrion membrane-related proteins and pathways.

3.3. Morphometric Analysis of RSV ON1-Infected Mitochondria in the HEP-2 Cells Line

Subsequently, morphometric measurements were performed in HEP-2 cells infected cells and compared to the mock-infected cells (Figure 3). The mitochondria surface area was used as a size descriptor, and 57 mitochondria from each time point were measured. The area of the control samples was examined over time. When comparing this shape descriptor as a function of time we only observed statistically significant differences at 2 and 48 h.p.i. (Figure 3A) (U-Mann Whitney). At 2-h.p.i. the mean mitochondria area was 0.18 ± 0.11 (\pm SD) μm^2 , at 24-h.p.i. the mean area to 0.57 ± 0.31 μm^2 . At two subsequent time points, the mean area did not change substantially: at 48- and 72-h.p.i the mean areas are 0.54 ± 0.32 μm^2 and 0.53 ± 0.30 μm^2 , respectively. Finally, at 96-h.p.i. the mean area decreased to 0.41 ± 0.24 μm^2 (Figure 3B). Using a Friedman test, we found a statistically significant difference between the area at 2-h.p.i. and the areas at each of the times of infection. In addition, we found a statistically significant difference between 24-h.p.i. and 96-h.p.i. when the area of the mitochondria decreases.

The mean mitochondrial area of the infected cells between the 2- and 48-h.p.i. 0.25 ± 0.18 μm^2 , 0.52 ± 0.42 μm^2 , and 0.71 ± 0.48 μm^2 . The area decreased at 72- and 96-h.p.i. the area was 0.57 ± 0.21 μm^2 and at 96-h.p.i. the area was 0.43 ± 0.23 μm^2 (Figure 3C). Using the

Friedman test, we found statistically significant differences between the mean area at 2-h.p.i. and the mean areas at each time of infection. In addition, we found a statistically significant difference between 48-h.p.i. and 96-h.p.i. when the area decreases in this last time point. These results indicate that in infected cells, the increase in area is sustained until 48-h.p.i. and after this, the mean area decreases as a function of time approaching that of the uninfected cells. We did not find statistical differences when comparing the mitochondrial area between both groups at most time points except for 2 and 48-h.p.i.

Another size descriptor, Feret's diameter, was used to confirm these findings. As with the surface area, there were statistically significant changes over time. In the mock-infected samples at 2-h.p.i. mitochondria Feret's diameter was 0.66 ± 0.29 (mean \pm SD) μm , at 24-h.p.i. the Feret's diameter increased to 1.1 ± 0.44 μm . However, at the following two time points, the diameter did not change substantially (1.1 ± 0.53 μm and 1.0 ± 0.42 μm , at 48- and 72-h.p.i.). Finally, at 96-h.p.i. the diameter decreased to 0.89 ± 0.35 μm (Figure 4A). Using the Friedman test, we found a statistically significant difference between the size at 2-h.p.i. and the sizes at each of the time points. In addition, we found a statistically significant difference between the 24- and 96-h.p.i. when the size decreases in this last time. These results indicate that in the control group, there was an increase in size from 24-h.p.i., the diameter was maintained over time and subsequently decreased in the last time of infection.

Figure 4A shows the differences in the Feret's diameter between groups at each time point and as in Figure 3A at 2 and 48 h.p.i. the differences between this shape descriptor are statistically significant (U-Mann Whitney). In the infected cells, the Feret's diameter at 2-h.p.i. was 0.78 ± 0.27 (mean \pm SD) μm , and at 24- and 48-h.p.i. the diameter increased to 1.1 ± 0.66 μm and 1.3 ± 0.72 μm , respectively. Finally, the diameter decreased at 72 and 96-h.p.i. from 1.1 ± 0.35 μm to 0.92 ± 0.36 μm , respectively (Figure 4B). Using the Friedman test, we found that there is a statistically significant difference between the size at 2-h.p.i. and the areas at each of the post infection times. In addition, we found that there is a statistically significant difference between the 48- and 96-h.p.i. when the size decreases in this last time. These findings suggest that hRSV ON1 infection is associated with an increase in mitochondrial size in Hep-2 cells that is different from the one observed in the control cells.

Finally, the complexity of mitochondria was evaluated by correlating two morphometric descriptors, the aspect ratio (AR) and the form factor (FF). In the first place, we compared the shape descriptors at 2-h.p.i. and found that the observed shapes of the mitochondria (i.e., round and elongated) in control and infected cells were not significantly different from one another (AR = 2.0 ± 0.88 vs. 2.3 ± 1.0 for infected cells; FF = 1.3 ± 0.31 vs. 1.4 ± 0.35 for infected cells). We found no statistically significant differences when the equations of the linear regressions for the

correlations were compared using the Student *t*-test for both groups. A value of $p > 0.05$ was obtained (Figure 5A).

However, at 24-h.p.i. (Figure 5B) we found that the correlations between AR and FF for the control and infected cells were significantly different from each other (AR = 1.7 ± 0.68 vs. 1.8 ± 0.68 for infected cells; FF = 1.2 ± 0.26 vs. 1.3 ± 0.44 for infected cells). Statistically significant differences were obtained when comparing the equations for the linear regression of both groups ($p < 0.001$). Figure 5B shows that in the infected groups at 24-h.p.i. the data points can be separated into two populations; one group of data points overlaps with all the data points of the mock-infected cells, while another group deviates considerably from this. This suggests that at this time point, there are two populations of mitochondria in the infected cells and one of them is more elongated than in the control cells.

At 48 h-post-infection (Figure 5C) there is a similar effect as 24-h.p.i. However, the differences between the infected and mock-infected samples are less pronounced than at the previous time point. The mean values for AR and FF observed that in both control and infected cells were significantly different in both groups (AR = 1.8 ± 1.1 vs. 1.8 ± 0.93 infected cells; FF = 1.2 ± 0.39 vs. 1.3 ± 0.42 for infected cells). We also found that in the infected cells, there is a population that is more elongated than in the controls. This can be seen by the data points that do not overlap with the control and by the fact that there is a statistically significant difference ($p < 0.001$) between the correlations for both samples. At 72- (Figure 5D) and 96-h.p.i. (Figure 5E) there are no statistically significant differences found when comparing the regression of the correlations. Overall, these findings indicate that RSV ON1 infection causes an increase in the size and elongation of mitochondria in HEp-2 cells at 24 and 48-h.p.i.

3.4. Effects of RSV ON1 Infection on HEp-2 Cell Line Mitochondrial Function Genes Expression

In order to determine if the changes in the mitochondria morphology are related to functional changes, we investigated if the infection with hRSV-ON1 is associated with alterations in homeostasis and mitochondrial function. Three mRNAs associated with mitochondrial function were analyzed: Mfn1, VDAC2, and PINK1. The Mfn1 gene encodes mitofusin 1, a protein related to mitochondrial outer membrane fusion. The VDAC2 gene encodes the voltage-dependent anion-selective channel 2, whose functions are related to oxidative metabolism and apoptosis. The PINK1 gene encode protein related to the process of mitophagy. The relative expression of these genes was normalized with GAPDH, and the Friedman test was performed for each group over time. Infection with hRSV ON1 resulted in downregulation of the Mfn1 (Figure 6), VDAC2 (Figure 7), and PINK1 (Figure 8) mRNAs. This expression was found to have a maximum in the infected group at 24-h.p.i. However, this expression is dramatically reduced at later time points. In the control group, the relative expression of these genes was constant.

In the case of the expression of PINK1 mRNA (Figure 8), there are no significant differences in the mock infected cells at different time points. However, in hRSV infected cells the expression of this mRNA is downregulated, specially at 48-, 60-, 72- and 96 h.p.i.

These data indicate that the expression of genes related to mitochondria elongation and apoptosis are down-regulated by hRSV infection, except during early stages of infection when transient overexpression of VDAC2 was observed. As such, it appears that hRSV-ON1 infection does not induce mitophagy.

4. Discussion

It has been previously documented that hRSV causes changes in the host cell's mitochondria that promote viral replication. In particular, previous studies show that mitochondria accumulate perinuclearly during early infection [24], while at the late infection stages the distribution near the microtubule organizing center is asymmetric [31]. Furthermore, hRSV infection has been shown to inhibit mitochondrial respiration, disrupt membrane potential, and increase reactive oxygen species production to promote viral replication [45]. These results demonstrate the importance of mitochondria during infection. However, few studies have examined changes in mitochondrial dynamics, including changes that affect the size, shape, and function of this organelle. To study the changes in mitochondrial dynamics, we used thin-section TEM and RT-qPCR to examine changes in mitochondrial structure and function induced by hRSV ON1 in Hep-2 cells.

We observed that the percentage of class 2 mitochondria in the mock-infected cells increased at 24- and 72-h.p.i. It is important to point out that at time 0-h.p.i the cells were incubated with either virus (in PBS) or PBS, and after two hours, the inoculum was replaced with complete DMEM. Also, the media was replaced after 48-h.p.i. Therefore, it is likely that the replacement of PBS with complete MDEM and/or the media replacement process could stress the cells, resulting in an increase in the percentage of Class 2 mitochondria at 24 and 72 h.p.i. Nonetheless, we found that, independently from these changes, hRSV ON1 induced changes in mitochondrial morphology by inducing outer membrane discontinuities, altering the shape of mitochondrial cristae, and inducing the formation of swirling or fragmented cristae. In contrast, the mitochondrial morphology of hRSV-uninfected cells did not change over time (mitochondria had clearly defined cristae and membranes).

While most studies with hRSV use MOIs between 0.1 and 3.0 [24,29–31,45,46] we decided to use an MOI of 10 to be able to detect ultrastructural changes, which is one of the limitations of this study. In previous studies with Zika (ZIKV) [47] and Chikungunya (CHIKV) [48] virus, we used low MOIs for thin-section TEM. However, preliminary experiments with hRSV at MOIs of 0.1 and 1.0 showed that detecting ultrastructural changes in the mitochondrion was

extremely challenging at these MOIs (data not shown). Furthermore, in the cases of CHIKV [48] and ZIKV [47] infections at an MOI of 1.0 lead to complete destruction of the cellular monolayer within the first 72 h.p.i.; however, with hRSV, infection at an MOI of 10 does not result in complete disruption of the monolayer even at 96-h.p.i. and hence, we sought to use a high MOI to increase the chance of finding ultrastructural changes. Nonetheless, our results consistent with published studies. In a previous study, hRSV was inoculated into guinea pig middle ears, and the infection generated swollen mitochondria in epithelial and mononuclear cells [49]. Another study showed mitochondrial damage in ciliated cells infected with hRSV [46]. Additionally, mitochondrial alterations have also been reported with other viruses, such as HCV [27] and SARS-CoV-2 [50]. Our findings suggest that hRSV ON1 alters mitochondrial morphology, especially the shape of mitochondrial membranes and cristae, during infection.

We then further examined the changes in mitochondrial morphology and quantified several shape descriptors. By evaluating the surface area, Feret's diameter, and complexity, we observed an increase in mitochondrial size due to elongation at early times. Based on our observations, we determined that hRSV-ON1 induces the formation of elongated mitochondria. On the hand, the frequency of damaged mitochondria increases with time and at 24- and 48-h.p.i. the morphology of the mitochondria in the infected cells is different compared to the mock-infected cells. On the other hand, the surface area and Feret's diameter are similar between infected and mock-infected cells. These observations suggest that, most likely, the class 3 and 4 mitochondria are degraded over time, and thus, in the later time points, we only detected class 1 and 2 mitochondria. This biases our observations toward healthy cells. Nonetheless, this could also indicate that hRSV-ON1 modulates mitochondrial dynamics to inhibit apoptosis and increase the chance of generating syncytia.

Previously, a study using confocal microscopy reported mitochondrial elongation in Hep-2 cells upon hRSV infection [51]. Elongation effects were also observed with MeV [51]. Furthermore, SARS-CoV promotes mitochondrial elongation in HEK293T and THP-1 cells through the expression of the viral accessory protein ORF-9b [52]. It has also been shown that dengue virus infection in hepatoma cells leads to mitochondrial elongation by decreasing phosphorylation of dynamin-related protein 1 (DRP1) [53]. Recently, H1N1 influenza virus was reported to induce a state of hyperelongated mitochondria in A549 cells; this effect was promoted by re-localization of the DRP1 protein [54]. Our results suggest that hRSV ON1 induces the formation of hyperfused mitochondria at early stages. However, the mechanism by which this induction occurs needs further investigation.

Given the fact that our morphometric analysis could be biased toward healthy cells or organelles (i.e., those that are too damaged can be hard to find), we sought to study the expression of mRNAs related to the function of the mitochondria. First, we investigated Mfn1,

which mediates mitochondrial outer membrane fusion through guanosine-5 hydrolysis-driven homo- and heterotypic interactions with triphosphate (GTP) [55]. This protein is essential for mitochondrial quality control and homeostasis, as well as for the regulation of numerous biological processes, including the immune response [56]. During viral infection, the immune response begins when viral RNA is detected in the cytosol by RIG-I-like receptors (RLRs), specifically RIG-1, which have two amino-terminal caspase activation and recruitment domains (CARDs); these domains interact with mitochondrial antiviral signaling protein, which are proteins of the mitochondrial outer membrane, and its activation is essential for initiating the production of type I interferons (IFN) and proinflammatory cytokines [57]. It has been reported that Mfn1 is required for efficient RLR signaling. When the RLRs are activated, Mfn1 promotes mitochondrial fusion/elongation. Conversely, when fusion is inhibited by Mfn1 silencing, activation of type I interferons (IFN) and pro-inflammatory cytokines decreases [58,59].

Our results showed that hRSV ON1 infection induces down-regulation of Mfn1 expression. These results might explain, in part, the shape and size descriptors described above. However, there is no direct evidence that mitochondrial elongation is related to Mfn1. In one study, Sirtuin 1 (SIRT1) was reported to regulate mitochondrial function in hRSV-infected dendritic cell [60]. The relationship between SIRT1 and Mfn1 has been previously studied and showed that mitochondrial elongation is regulated by SIRT1-mediated stabilization of Mfn1 [61]. On the one hand, this could indicate the role of Mfn1 as a modulator of the immune response to viral infections. However, more studies are needed to confirm this association. On the other hand, in other viruses, such as dengue virus [62] and measles virus [51], the relationship between hyperfusion and Mfn1 expression during the infection processes has been directly studied.

The expression of mRNA for VDAC, the most abundant mitochondrial membrane protein, was also evaluated in its isoform 2 (VDAC2). This protein is involved in a wide range of processes, such as the passage of ATP outside the mitochondria, the release of anions superoxide, as well as in the apoptosis process [63]. One of the roles of the VDAC2 protein is to regulate the apoptosis process through the release of pro-apoptotic factors such as cytochrome C. It has been described that increased membrane permeability induced by VDAC2 overexpression could mediate cytochrome C release. This leads to the activation of caspases, proteolytic enzymes which are key proteins in the apoptotic process [64]. The relevance of this protein and its manipulation could have significant implications during viral infection. The quantification of VDAC2 mRNA showed a transient upregulation in early stages of infection, while notable downregulation occurred at later stages of infection. This behavior is similar to the one we found for Mfn1.

Previous studies have described that the hRSV M protein interacts with the VDAC protein. However, the exact molecular mechanism of this interaction and its effect on RSV replication are

still unknown [29]. Furthermore, a previous study analyzing the mitochondrial proteome during hRSV infection in A549 cells found that the levels of different isoforms of the VDAC were significantly increased during the late stages of infection [30]. As another example, influenza virus PB1-F2 protein induces cell death through VDAC1. Although the induction of apoptosis by influenza virus may appear to be contradictory for efficient viral production, it is critical for influenza viral replication [65]. Our results are inconsistent with these previous studies, as we observed downregulation in late times of the infection. Apoptosis-related signaling pathways are inhibited by hRSV infection, which may be its survival strategy. More research is needed to understand the relationship between all of our observations.

PINK1 is a key mediator of mitochondrial quality control processes and activates the mitophagy process [66]. Unlike the expression of the previously described genes (Mfn1 and VDAC2), PINK1 down-regulation was less notable. PINK1 expression downregulation has been described previously. hRSV infection in mice primary peritoneal macrophages induces PINK1 downregulation. This same phenomenon was also observed when studying infection with vesicular stomatitis virus and herpes simplex virus [67]. These results indicated that PINK1 mRNA was downregulated following hRSV ON1 infection. This may indicate that hRSV ON1 infection inhibits the PINK1/Parkin-dependent mitophagy pathway. However, more research is needed to allow us to understand the mechanism of this inhibitory effect. To further understand this inhibitory effect, it is important to consider the dynamics of the PINK1/Parkin-dependent mitophagy pathway.

On the one hand, most of the ultrastructural changes were only noticeable in early times, before there was an exponential growth in viral RNA (see Supplementary Figure S2). This could be due to the expression of early viral genes. At this stage it is unclear which genes are involved in these changes as there is a debate about whether hRSV gene expression follows a gradient or a steady-state regime [68,69]. Also, it seems to be a slight up-regulation of VDAC2 and Mfn1 only at early times, correlating almost perfectly with the alterations seen in Figure 5, before these genes are strongly down-regulated. On the other hand, at time points close and before the maximum viremia, most mitochondria have a normal morphology. This suggests that the downregulation of VDAC2, Mfn1, and PINK could be an indirect consequence of virus-induced cellular death, thus we were not able to observe abnormal mitochondria at these time points. It is important to point out that even at the peak of the viremia, we were not able to observe the complete destruction of the monolayer. Therefore, the lack of monolayer destruction and the abrupt drop in viremia at 72-h.p.i. suggest that the downregulation of VDAC2, Mfn1, and PINK might be an antiviral response that limits the progression of the infection and therefore at these time points most mitochondria have normal morphology.

5. Conclusions

This study provides evidence that hRSV-A ON1 infection induces significant changes in mitochondrial morphology and function in HEp-2 cells. The changes in mitochondrial size, cristae damage, and loss of membrane integrity indicate aberrant mitochondrial dynamics. The results show that hRSV infection promotes downregulation of several genes that are key for mitochondrial function. In addition, the study suggests that alterations in mitochondrial dynamics may impair antiviral signaling pathways and mitophagy and contribute to hRSV pathogenesis. These results shed light on the complex interplay between hRSV and mitochondria and offer potential targets for therapeutic interventions. The results of this study are promising as they can serve as a basis for the development of new antiviral therapies to combat hRSV. Further research is needed to determine how these findings can be used to improve the management of hRSV.

References

1. Schoch, C.L.; Ciufo, S.; Domrachev, M.; Hotton, C.L.; Kannan, S.; Khovanskaya, R.; Leipe, D.; McVeigh, R.; O'Neill, K.; Robbertse, B.; et al. NCBI Taxonomy: A comprehensive update on curation, resources and tools. *Database* **2020**, *2020*, baaa062. [CrossRef] [PubMed]
2. Li, Y.; Wang, X.; Blau, D.M.; Caballero, M.T.; Feikin, D.R.; Gill, C.J.; Madhi, S.A.; Omer, S.B.; Simões, E.A.F.; Campbell, H.; et al. Global, regional, and national disease burden estimates of acute lower respiratory infections due to respiratory syncytial virus in children younger than 5 years in 2019: A systematic analysis. *Lancet* **2022**, *399*, 2047–2064. [CrossRef] [PubMed]
3. Johnson, P.R.; Spriggs, M.K.; Olmsted, R.A.; Collins, P.L. The G glycoprotein of human respiratory syncytial viruses of subgroups A and B: Extensive sequence divergence between antigenically related proteins. *Proc. Natl. Acad. Sci. USA* **1987**, *84*, 5625–5629. [CrossRef] [PubMed]
4. Battles, M.B.; McLellan, J.S. Respiratory syncytial virus entry and how to block it. *Nat. Rev. Microbiol.* **2019**, *17*, 233–245. [CrossRef]
5. García, O.; Martín, M.; Dopazo, J.; Arbiza, J.; Frabasile, S.; Russi, J.; Hortal, M.; Perez-Breña, P.; Martínez, I.; García-Barreno, B. Evolutionary pattern of human respiratory syncytial virus (subgroup A): Cocirculating lineages and correlation of genetic and antigenic changes in the G glycoprotein. *J. Virol.* **1994**, *68*, 5448–5459. [CrossRef]
6. Trento, A.; Galiano, M.; Videla, C.; Carballal, G.; García-Barreno, B.; Melero, J.A.; Palomo, C. Major changes in the G protein of human respiratory syncytial virus isolates introduced by a duplication of 60 nucleotides. *J. Gen. Virol.* **2003**, *84*, 3115–3120. [CrossRef]

7. Muñoz-Escalante, J.C.; Comas-García, A.; Bernal-Silva, S.; Noyola, D.E. Respiratory syncytial virus B sequence analysis reveals a novel early genotype. *Sci. Rep.* **2021**, *11*, 3452. [CrossRef]
8. Eshaghi, A.; Duvvuri, V.R.; Lai, R.; Nadarajah, J.T.; Li, A.; Patel, S.N.; Low, D.E.; Gubbay, J.B. Genetic Variability of Human Respiratory Syncytial Virus A Strains Circulating in Ontario: A Novel Genotype with a 72 Nucleotide G Gene Duplication. *PLoS ONE* **2012**, *7*, e32807. [CrossRef]
9. Comas-García, A.; Noyola, D.E.; Cadena-Mota, S.; Rico-Hernández, M.; Bernal-Silva, S. Respiratory Syncytial Virus-A ON1 Genotype Emergence in Central Mexico in 2009 and Evidence of Multiple Duplication Events. *J. Infect. Dis.* **2018**, *217*, 1089–1098. [CrossRef]
10. Cantú-Flores, K.; Rivera-Alfaro, G.; Muñoz-Escalante, J.C.; Noyola, D.E. Global distribution of respiratory syncytial virus A and B infections: A systematic review. *Pathog. Glob. Health* **2022**, *116*, 398–409. [CrossRef]
11. Miller, S.; Krijnse-Locker, J. Modification of intracellular membrane structures for virus replication. *Nat. Rev. Microbiol.* **2008**, *6*, 363–374. [CrossRef] [PubMed]
12. de Armas-Rillo, L.; Valera, M.-S.; Marrero-Hernández, S.; Valenzuela-Fernández, A. Membrane dynamics associated with viral infection. *Rev. Med. Virol.* **2016**, *26*, 146–160. [CrossRef] [PubMed]
13. Romero-Brey, I.; Bartenschlager, R. Membranous Replication Factories Induced by Plus-Strand RNA Viruses. *Viruses* **2014**, *6*, 2826–2857. [CrossRef] [PubMed]
14. Cowton, V.M.; Fearn, R. Evidence that the respiratory syncytial virus polymerase is recruited to nucleotides 1 to 11 at the 3⁰ end of the nucleocapsid and can scan to access internal signals. *J. Virol.* **2005**, *79*, 11311–11322. [CrossRef]
15. Ghildyal, R.; Li, D.; Peroulis, I.; Shields, B.; Bardin, P.G.; Teng, M.N.; Collins, P.L.; Meanger, J.; Mills, J. Interaction between the respiratory syncytial virus G glycoprotein cytoplasmic domain and the matrix protein. *J. Gen. Virol.* **2005**, *86 Pt 7*, 1879–1884. [CrossRef]
16. Ghildyal, R.; Mills, J.; Murray, M.; Vardaxis, N.; Meanger, J. Respiratory syncytial virus matrix protein associates with nucleocapsids in infected cells. *J. Gen. Virol.* **2022**, *83 Pt 4*, 753–757. [CrossRef]
17. Reimers, K.; Buchholz, K.; Werchau, H. Respiratory syncytial virus M2-1 protein induces the activation of nuclear factor kappa B. *Virology* **2005**, *331*, 260–268. [CrossRef]
18. Li, D.; Jans, D.A.; Bardin, P.G.; Meanger, J.; Mills, J.; Ghildyal, R. Association of respiratory syncytial virus M protein with viral nucleocapsids is mediated by the M2-1 protein. *J. Virol.* **2008**, *82*, 8863–8870. [CrossRef]

19. Li, H.M.; Ghildyal, R.; Hu, M.; Tran, K.C.; Starrs, L.M.; Mills, J.; Teng, M.N.; Jans, D.A. Respiratory Syncytial Virus Matrix Protein-Chromatin Association Is Key to Transcriptional Inhibition in Infected Cells. *Cells* **2021**, *10*, 2786. [CrossRef]
20. Bossert, B.; Marozin, S.; Conzelmann, K.K. Nonstructural proteins NS1 and NS2 of bovine respiratory syncytial virus block activation of interferon regulatory factor 3. *J. Virol.* **2003**, *77*, 8661–8668. [CrossRef]
21. Elliott, J.; Lynch, O.T.; Suessmuth, Y.; Qian, P.; Boyd, C.R.; Burrows, J.F.; Buick, R.; Stevenson, N.J.; Touzelet, O.; Gadina, M.; et al. Respiratory syncytial virus NS1 protein degrades STAT2 by using the Elongin-Cullin E3 ligase. *J. Virol.* **2007**, *81*, 3428–3436. [CrossRef] [PubMed]
22. Bhoj, V.G.; Sun, Q.; Bhoj, E.J.; Somers, C.; Chen, X.; Torres, J.P.; Mejias, A.; Gomez, A.M.; Jafri, H.; Ramilo, O.; et al. MAVS and MyD88 are essential for innate immunity but not cytotoxic T lymphocyte response against respiratory syncytial virus. *Proc. Natl. Acad. Sci. USA* **2008**, *105*, 14046–14051. [CrossRef] [PubMed]
23. Lifland, A.W.; Jung, J.; Alonas, E.; Zurla, C.; Crowe, J.E., Jr.; Santangelo, P.J. Human respiratory syncytial virus nucleoprotein and inclusion bodies antagonize the innate immune response mediated by MDA5 and MAVS. *J. Virol.* **2012**, *86*, 8245–8258. [CrossRef]
24. Hu, M.; Li, H.M.; Bogoyevitch, M.A.; Jans, D.A. Mitochondrial protein p32/HAPB1/gC1qR/C1qbp is required for efficient respiratory syncytial virus production. *Biochem. Biophys. Res. Commun.* **2017**, *489*, 460–465. [CrossRef]
25. Kim, S.-J.; Ahn, D.-G.; Syed, G.H.; Siddiqui, A. The essential role of mitochondrial dynamics in antiviral immunity. *Mitochondrion* **2017**, *41*, 21–27. [CrossRef]
26. Kim, S.-J.; Syed, G.H.; Khan, M.; Chiu, W.-W.; Sohail, M.A.; Gish, R.G.; Siddiqui, A. Hepatitis C virus triggers mitochondrial fission and attenuates apoptosis to promote viral persistence. *Proc. Natl. Acad. Sci. USA* **2014**, *111*, 6413–6418. [CrossRef]
27. Kim, S.-J.; Syed, G.H.; Siddiqui, A. Hepatitis C Virus Induces the Mitochondrial Translocation of Parkin and Subsequent Mitophagy. *PLoS Pathog.* **2013**, *9*, e1003285. [CrossRef] [PubMed]
28. Xia, M.; Gonzalez, P.; Li, C.; Meng, G.; Jiang, A.; Wang, H.; Gao, Q.; Debatin, K.-M.; Beltinger, C.; Wei, J. Mitophagy enhances oncolytic measles virus replication by mitigating DDX58/RIG-I-like receptor signaling. *J. Virol.* **2014**, *88*, 5152–5164. [CrossRef]
29. Kipper, S.; Hamad, S.; Caly, L.; Avrahami, D.; Bacharach, E.; Jans, D.A.; Gerber, D.; Bajorek, M. New host factors important for respiratory syncytial virus (RSV) replication revealed by a novel microfluidics screen for interactors of matrix (M) protein. *Mol. Cell. Proteom.* **2015**, *14*, 532–543. [CrossRef]

30. Munday, D.C.; Howell, G.; Barr, J.N.; Hiscox, J.A. Proteomic analysis of mitochondria in respiratory epithelial cells infected with human respiratory syncytial virus and functional implications for virus and cell biology. *J. Pharm. Pharmacol.* **2015**, *67*, 300–318. [CrossRef]
31. Hu, M.; Schulze, K.E.; Ghildyal, R.; Henstridge, D.C.; Kolanowski, J.L.; New, E.J.; Hong, Y.; Hsu, A.C.; Hansbro, P.M.; Wark, P.A.; et al. Respiratory syncytial virus co-opts host mitochondrial function to favour infectious virus production. *eLife* **2019**, *8*, e42448. [CrossRef] [PubMed]
32. Comas-García, A.; López-Pacheco, C.P.; García-Zepeda, E.A.; Soldevila, G.; Ramos-Martínez, P.; Ramos-Castañeda, J. Neonatal respiratory syncytial virus infection has an effect on lung inflammation and the CD4⁺ CD25⁺ T cell subpopulation during ovalbumin sensitization in adult mice. *Clin. Exp. Immunol.* **2016**, *185*, 190–201. [CrossRef] [PubMed]
33. Martínez, I.; Lombardía, L.; Herranz, C.; García-Barreno, B.; Domínguez, O.; Melero, J.A. Cultures of HEp-2 cells persistently infected by human respiratory syncytial virus differ in chemokine expression and resistance to apoptosis as compared to lytic infections of the same cell type. *Virology* **2009**, *388*, 31–41. [CrossRef]
34. McKimm-Breschkin, J.L. A simplified plaque assay for respiratory syncytial virus—Direct visualization of plaques without immunostaining. *J. Virol. Methods* **2004**, *120*, 113–117. [CrossRef]
35. King, T.; Mejias, A.; Ramilo, O.; Peeples, M.E. The larger attachment glycoprotein of respiratory syncytial virus produced in primary human bronchial epithelial cultures reduces infectivity for cell lines. *PLoS Pathog.* **2021**, *17*, e1009469. [CrossRef] [PubMed]
36. Boyapalle, S.; Wong, T.; Garay, J.; Teng, M.; San Juan-Vergara, H.; Mohapatra, S.; Mohapatra, S. Respiratory syncytial virus NS1 protein colocalizes with mitochondrial antiviral signaling protein MAVS following infection. *PLoS ONE* **2012**, *7*, e29386. [CrossRef] [PubMed]
37. Bossert, B.; Conzelmann, K.K. Respiratory syncytial virus (RSV) nonstructural (NS) proteins as host range determinants: A chimeric bovine RSV with NS genes from human RSV is attenuated in interferon-competent bovine cells. *J. Virol.* **2002**, *76*, 4287–4293. [CrossRef]
38. Rayaprolu, V.; Ramsey, J.; Wang, J.C.; Mukhopadhyay, S. Alphavirus Purification Using Low-speed Spin Centrifugation. *BioProtocol* **2018**, *8*, e2772. [CrossRef]
39. Tobin, G.J.; Nagashima, K.; Gonda, M.A. Immunologic and Ultrastructural Characterization of HIV Pseudovirions Containing Gag and Env Precursor Proteins Engineered in Insect Cells. *Methods* **1996**, *10*, 208–218. [CrossRef]
40. Crouser, E.D.; Julian, M.W.; Dorinsky, P.M. Ileal VO(2)-O(2) alterations induced by endotoxin correlate with severity of mitochondrial injury. *Am. J. Respir. Crit. Care Med.* **1999**, *160*, 1347–1353. [CrossRef]

41. Joshi, M.S.; Crouser, E.D.; Julian, M.W.; Schanbacher, B.L.; Bauer, J.A. Digital imaging analysis for the study of endotoxin-induced mitochondrial ultrastructure injury. *Anal. Cell. Pathol.* **2000**, *21*, 41–48. [CrossRef] [PubMed]
42. Livak, K.J.; Schmittgen, T.D. Analysis of relative gene expression data using real-time quantitative PCR and the $2^{-\Delta\Delta C(T)}$ Method. *Methods* **2001**, *25*, 402–408. [CrossRef] [PubMed]
43. Chiok, K.; Pokharel, S.M.; Mohanty, I.; Miller, L.G.; Gao, S.J.; Haas, A.L.; Tran, K.C.; Teng, M.N.; Bose, S. Human Respiratory Syncytial Virus NS2 Protein Induces Autophagy by Modulating Beclin1 Protein Stabilization and ISGylation. *mBio* **2022**, *13*, e0352821. [CrossRef] [PubMed]
44. Raiden, S.; Sananez, I.; Remes-Lenicov, F.; Pandolfi, J.; Romero, C.; De Lillo, L.; Ceballos, A.; Geffner, J.; Arruvito, L. Respiratory Syncytial Virus (RSV) Infects CD4+ T Cells: Frequency of Circulating CD4+ RSV+ T Cells as a Marker of Disease Severity in Young Children. *J. Infect. Dis.* **2017**, *215*, 1049–1058. [CrossRef] [PubMed]
45. Hu, M.; Bogoyevitch, M.A.; Jans, D.A. Subversion of Host Cell Mitochondria by RSV to Favor Virus Production depends on the Inhibition of Mitochondrial Complex I and ROS Generation. *Cells* **2019**, *8*, 1417. [CrossRef]
46. Smith, C.M.; Kulkarni, H.; Radhakrishnan, P.; Rutman, A.; Bankart, M.J.; Williams, G.; Hirst, R.A.; Easton, A.J.; Andrew, P.W.; O'Callaghan, C. Ciliary dyskinesia is an early feature of respiratory syncytial virus infection. *Eur. Respir. J.* **2014**, *43*, 485–496. [CrossRef]
47. Rubio-Hernández, E.I.; Comas-García, M.; Coronado-Ipiña, M.A.; Colunga-Saucedo, M.; González Sánchez, H.M.; Castillo, C.G. Astrocytes derived from neural progenitor cells are susceptible to Zika virus infection. *PLoS ONE* **2023**, *18*, e0283429. [CrossRef] [PubMed]
48. Colunga-Saucedo, M.; Rubio-Hernandez, E.I.; Coronado-Ipiña, M.A.; Rosales-Mendoza, S.; Castillo, C.G.; Comas-García, M. Construction of a Chikungunya Virus, Replicon, and Helper Plasmids for Transfection of Mammalian Cells. *Viruses* **2022**, *15*, 132. [CrossRef]
49. Zhong, G.Y. Ultrastructural changes in middle ear and cochlea caused by respiratory syncytial virus in guinea pigs. *Zhonghua Er Bi Yan Hou Ke Za Zhi* **1990**, *25*, 213–215, 255.
50. Cortese, M.; Lee, J.-Y.; Cerikan, B.; Neufeldt, C.J.; Oorschot, V.M.J.; Köhrer, S.; Hennies, J.; Schieber, N.L.; Ronchi, P.; Mizzon, G.; et al. Integrative Imaging Reveals SARS-CoV-2-Induced Reshaping of Subcellular Morphologies. *Cell Host Microbe* **2020**, *28*, 853–866.e5. [CrossRef]
51. Sato, H.; Hoshi, M.; Ikeda, F.; Fujiyuki, T.; Yoneda, M.; Kai, C. Downregulation of mitochondrial biogenesis by virus infection triggers antiviral responses by cyclic GMP-AMP synthase. *PLoS Pathog.* **2021**, *17*, e1009841. [CrossRef]

52. Shi, C.-S.; Qi, H.-Y.; Boullaran, C.; Huang, N.-N.; Abu-Asab, M.; Shelhamer, J.H.; Kehrl, J.H. SARS-coronavirus open reading frame-9b suppresses innate immunity by targeting mitochondria and the MAVS/TRAF3/TRAF6 signalosome. *J. Immunol.* **2014**, *193*, 3080–3089. [CrossRef] [PubMed]
53. Chatel-Chaix, L.; Cortese, M.; Romero-Brey, I.; Bender, S.; Neufeldt, C.J.; Fischl, W.; Scaturro, P.; Schieber, N.; Schwab, Y.; Fischer, B.; et al. Dengue Virus Perturbs Mitochondrial Morphodynamics to Dampen Innate Immune Responses. *Cell Host Microbe* **2016**, *20*, 342–356. [CrossRef] [PubMed]
54. Pila-Castellanos, I.; Molino, D.; McKellar, J.; Lines, L.; Da Graca, J.; Tauziet, M.; Chanteloup, L.; Mikaelian, I.; Meyniel-Schicklin, L.; Codogno, P.; et al. Mitochondrial morphodynamic alteration induced by influenza virus infection as a new antiviral strategy. *PLoS Pathog.* **2021**, *17*, e1009340. [CrossRef]
55. Brandt, T.; Cavellini, L.; Kühlbrandt, W.; Cohen, M.M. A mitofusin-dependent docking ring complex triggers mitochondrial fusion in vitro. *eLife* **2016**, *5*, e14618. [CrossRef] [PubMed]
56. Xian, H.; Liou, Y.C. Functions of outer mitochondrial membrane proteins: Mediating the crosstalk between mitochondrial dynamics and mitophagy. *Cell Death Differ.* **2020**, *28*, 827–842. [CrossRef]
57. Kawai, T.; Akira, S. Toll-like Receptor and RIG-1-like Receptor Signaling. *Ann. N. Y. Acad. Sci.* **2008**, *1143*, 1–20. [CrossRef]
58. Castanier, C.; Garcin, D.; Vazquez, A.; Arnoult, D. Mitochondrial dynamics regulate the RIG-I-like receptor antiviral pathway. *EMBO Rep.* **2009**, *11*, 133–138. [CrossRef]
59. Onoguchi, K.; Onomoto, K.; Takamatsu, S.; Jogi, M.; Takemura, A.; Morimoto, S.; Julkunen, I.; Namiki, H.; Yoneyama, M.; Fujita, T. Virus-Infection or 5⁰ppp-RNA Activates Antiviral Signal through Redistribution of IPS-1 Mediated by MFN1. *PLoS Pathog.* **2010**, *6*, e1001012. [CrossRef]
60. Elesela, S.; Morris, S.B.; Narayanan, S.; Kumar, S.; Lombard, D.B.; Lukacs, N.W. Sirtuin 1 regulates mitochondrial function and immune homeostasis in respiratory syncytial virus infected dendritic cells. *PLoS Pathog.* **2020**, *16*, e1008319. [CrossRef]
61. Oanh, N.T.K.; Park, Y.-Y.; Cho, H. Mitochondria elongation is mediated through SIRT1-mediated MFN1 stabilization. *Cell. Signal.* **2017**, *38*, 67–75. [CrossRef] [PubMed]
62. Yu, C.-Y.; Liang, J.-J.; Li, J.-K.; Lee, Y.-L.; Chang, B.-L.; Su, C.-I.; Huang, W.-J.; Lai, M.M.C.; Lin, Y.-L. Dengue Virus Impairs Mitochondrial Fusion by Cleaving Mitofusins. *PLoS Pathog.* **2015**, *11*, e1005350. [CrossRef] [PubMed]
63. Gonçalves, R.P.; Buzhynskyy, N.; Prima, V.; Sturgis, J.N.; Scheuring, S. Supramolecular Assembly of VDAC in Native Mitochondrial Outer Membranes. *J. Mol. Biol.* **2007**, *369*, 413–418. [CrossRef]

64. Shoshan-Barmatz, V.; Keinan, N.; Zaid, H. Uncovering the role of VDAC in the regulation of cell life and death. *J. Bioenerg. Biomembr.* **2008**, *40*, 183–191. [CrossRef]
65. Zamarin, D.; García-Sastre, A.; Xiao, X.; Wang, R.; Palese, P. Influenza Virus PB1-F2 Protein Induces Cell Death through Mitochondrial ANT3 and VDAC1. *PLoS Pathog.* **2005**, *1*, e4. [CrossRef]
66. Li, Y.; Wu, K.; Zeng, S.; Zou, L.; Li, X.; Xu, C.; Li, B.; Liu, X.; Li, Z.; Zhu, W.; et al. The Role of Mitophagy in Viral Infection. *Cells* **2022**, *11*, 711. [CrossRef]
67. Zhou, J.; Yang, R.; Zhang, Z.; Liu, Q.; Zhang, Y.; Wang, Q.; Yuan, H. Mitochondrial Protein PINK1 Positively Regulates RLR Signaling. *Front. Immunol.* **2019**, *10*, 1069. [CrossRef] [PubMed]
68. Boukhvalova, M.S.; Prince, G.A.; Blanco, J.C.G. Respiratory Syncytial Virus Infects and Abortively Replicates in the Lungs in Spite of Preexisting Immunity. *J. Virol.* **2007**, *81*, 9443–9450. [CrossRef]
69. Piedra, F.-A.; Qiu, X.; Teng, M.N.; Avadhanula, V.; Machado, A.A.; Kim, D.-K.; Hixson, J.; Bahl, J.; Piedra, P.A. Non-gradient and genotype-dependent patterns of RSV gene expression. *PLoS ONE* **2020**, *15*, e0227558. [CrossRef]

Tables

Table 1. Design of primers for real-time PCR.

Gene	Primer's Sequence (5'-3')
PINK1 forward	GAGTATGGAGCAGTCACTTACAG
PINK1 reverse	CAGCACATCAGGGTAGTCG
Mfn1 forward	ACCTGTTTCTCCACTGAAGC
Mfn1 reverse	TGGCTATTCGATCAAGTTCCG
VDAC2 forward	TGTCTTTGGTTATGAGGGCTG
VDAC2 reverse	CCTCCAAATTCTGTCCCATCG
GAPDH forward	CAAGGCTGAGAACGGGAAGC
GAPDH reverse	AGGGGGCAGAGATGATGACC
MCVF	GGCAAATATGGAAACATACGTGAA
MCVR	TCTTTTTCTAGGACATTGTAYTGAACA

Table 2. Qualitative scoring system [40,41].

Injury Stage	Characteristics of Mitochondria
Class I	Mitochondria are considered normal. The cristae are densely packed and longitudinal, and the matrix is electron dense.
Class II	Mitochondria in this class have rounded or asymmetrical cristae. The cristae's direction, narrowness, or regular distribution have been lost.
Class III	Mitochondria vary in size and form, with discontinuous membranes, fragmented cristae, and swollen and electro lucent matrix.
Class IV	In this class, the mitochondrial double membrane is no longer complete, and the cristae are disrupted and dispersed.

Figure captions

Figure 1. Representative micrographs of the ultrastructural characterization of mitochondria from hRSV ON1-infected HEp-2 cells. **(A–D)** Mock-infected samples at different time points (2-, 24-, 48-, 72-h.p.i. respectively). In these micrographs the mitochondrial morphology is maintained, the mitochondrial membrane is intact, maintaining the inner and outer membrane (arrowhead), and the mitochondrial cristae are transversely oriented (asterisks). On the contrary **(E–H)** show the infected cells at different time points (2-, 24-, 48-, 72-h.p.i. respectively) and there are different degrees of damage. **(E)** There are swirling cristae, which have lost their length and are no longer found transversally (asterisk). the mitochondrial membrane is intact (arrowhead). **(F)** The mitochondrial membrane is diffuse (arrow), a swollen matrix with shortened and diffuse cristae (asterisk). **(G)** There is damage to mitochondrial cristae, which have lost their length and are shortened. Finally, in **(H)** there are swirling cristae with shortened length (asterisks). The scale bar corresponds to 0.5 μ m in the control and 0.75 μ m in the infected.

Figure 2. Representative micrographs illustrating the sorting of mitochondria from hRSV ON1-infected HEp-2 cells. Representative thin-section TEM micrographs according to the level of abnormality into four classes: class I (**A**) is characterized by having a defined membrane (arrowhead), in addition to transversely oriented cristae (asterisk); class II (**B**) is defined by a conserved membrane (arrowhead), but there is damage at the level of cristae that are shortened or swirled (asterisk); class III (**C**) corresponds to a mitochondrion with fragmented cristae (asterisk) and damaged membrane (arrow); and class IV (**D**) corresponds to the mitochondria with outer membrane broken and discontinuous (arrow) as well as deficient cristae (asterisk). (**E**) In the control cells, class I mitochondria predominates over time. (**F,G**) In contrast, in RSV ON1-infected cells there is a predominance of class II and class III mitochondria. (**H**) There are only a few mitochondria class IV both groups; however, there is a higher frequency of this class in the infected group at 48 -and 96-h.p.i. Fisher's exact test was performed for each class and the statistically significant differences are shown as an asterisk above the diagrams * corresponds to $p \leq 0.03$, ** $p \leq 0.002$, *** $p \leq 0.0002$ and **** $p \leq 0.0001$. Each sample was done in duplicate.

Figure 3. Morphometric analysis of the surface area of mitochondria represented in box plots. The surface area was compared between times points (**A**), and within groups at different times post infections. (**B**) The group of the control HEp-2 cells ($n = 57$) is represented in a blue boxplot, and (**C**) the group of the HEp-2 cells infected with the hRSV ON1 MOI = 10 ($n = 57$) represented in a light brown color box plot. Data were analyzed using the Friedman test and statistically significant differences are shown in the form of an asterisk above the box plots, * corresponds to $p \leq 0.03$, ** corresponds to $p \leq 0.002$, and **** corresponds to $p \leq 0.0001$. A U-Mann Whitney test was performed for the comparison between the control and infected group at each of the time post infection. The bars indicate the data between the lower quartile (25%) and the lower extreme and the upper quartiles (75%) and the upper extreme.

Figure 4. Morphometric analysis of the Feret's diameter of mitochondria represented in box plots. (**A**) Feret's diameter was compared between time points, and within groups at the different times post infection, the group of the control HEp-2 cells ($n = 57$) represented in a blue box plot (**B**) and the group of the HEp-2 cells infected with hRSV ON1 MOI10 ($n = 57$) represented in a light brown box plot (**C**). Data were analyzed using the Friedman test and statistically significant differences are shown in the form of an asterisk above the box plots * corresponds to $p \leq 0.03$, ** corresponds to $p \leq 0.002$, and **** corresponds to $p \leq 0.0001$. A U-Mann Whitney test was performed for the comparison between the control and infected group at each of the time post infection. The bars indicate the data between the lower quartile (25%) and the lower extreme and the upper quartiles (75%) and the upper extreme.

Figure 5. Mitochondrial complexity analysis. The complexity of mitochondria was evaluated by comparing the shape factor and aspect ratio at different times post infection (**A–E**). Control HEp-2 cells ($n = 57$) represented by the blue line, and HEp-2 cells infected with hRSV ON1 MOI10 ($n = 57$), represented by the orange line, were used. A two-sided Student's *t*-test was performed to compare the equations of the post-infection timeline, and the *p*-values are shown on the graph.

Figure 6. Evaluation of the relative expression of Mfn1 mRNA. The relative expression of the Mfn1 gene, normalized with GAPDH, was measured in control HEp-2 cells (blue boxes) and HEp-2 cells infected with ON1 respiratory syncytial virus (brown boxes). (**A**) Comparison of the relative expression of Mfn1 mRNA compared within time points, and within groups (**B**) and (**C**). Data are expressed as means and interquartile ranges; $n = 6$ per group. Friedman's test was performed for each of the groups at different times post-infection, and statistically significant differences are indicated with an asterisk above the boxplots, * corresponds to $p \leq 0.03$, ** corresponds to $p \leq 0.002$, *** corresponds to $p \leq 0.0002$ and **** corresponds to $p \leq 0.0001$. A U-Mann Whitney test was performed for the comparison between the control and infected group at each of the time post infection. The bars indicate the data between the lower quartile (25%) and the lower extreme and the upper quartiles (75%) and the upper extreme.

Figure 7. Evaluation of the relative expression of VDAC2 mRNAs. The relative expression of the VDAC2 gene, normalized with GAPDH, was in control HEP-2 cells (blue boxes) and HEP-2 cells infected with ON1 respiratory syncytial virus (brown boxes). (A) Comparison of the relative expression of Mfn1 mRNA compared within time points, and within groups (B) and (C). Data are expressed as means and interquartile ranges; $n = 6$ per group. Friedman's test was performed for each of the groups at different times post-infection, and statistically significant differences are indicated with an asterisk above the boxplots, * corresponds to $p \leq 0.03$, ** corresponds to $p \leq 0.002$, *** corresponds to $p \leq 0.0002$ and **** corresponds to $p \leq 0.0001$. A U-Mann Whitney test was performed for the comparison between the control and infected group at each of the time post infection. The bars indicate the data between the lower quartile (25%) and the lower extreme and the upper quartiles (75%) and the upper extreme.

Figure 8. Evaluation of the relative expression of PINK1 mRNAs. The relative expression of the PINK1 gene, normalized with GAPDH, was measured in control HEP-2 cells (blue boxes) and HEP-2 cells infected with ON1 respiratory syncytial virus (brown boxes). (A) Comparison of the relative expression of Mfn1 mRNA compared within time points, and within groups (B) and (C). Data are expressed as means and interquartile ranges; $n = 6$ per group. Friedman's test was performed for each of the groups at different times post-infection, and no statistically significant differences were found. A U-Mann Whitney test was performed for the comparison between the control and infected group at each of the time post infection; statistically significant differences are indicated with an asterisk above the boxplots, * corresponds to $p \leq 0.03$, ** corresponds to $p \leq 0.002$, *** corresponds to $p \leq 0.0002$ and **** corresponds to $p \leq 0.0001$. The bars indicate the data between the lower quartile (25%) and the lower extreme and the upper quartiles (75%) and the upper extreme.

Figure S1. Fold-change in GAPDH expression between infected and uninfected cells. The fold change in gene expression was calculated using the $2^{-\Delta Ct}$ method. The values represent mean fold change with standard deviation. No statistically significant relationship exists between infected and uninfected cell expression of GAPDH.

Figure S2. Kinetics of RSV ON1 infection in vitro assays. Hep-2 cell monolayers were infected with hRSV ON1 at a multiplicity of infection (MOI) 10. At various times post-infection, total virus (copy/uL) in the total RNA were determined. In each assay, the experimental data (circles) were collected in duplicate (MOI 10).

Figure 1

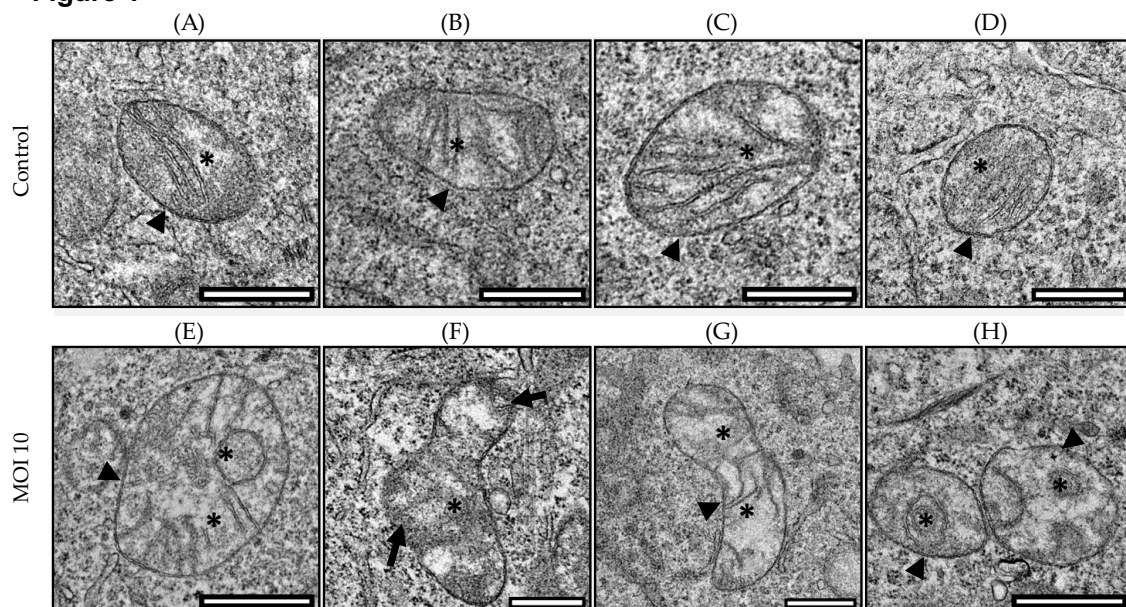


Figure 2

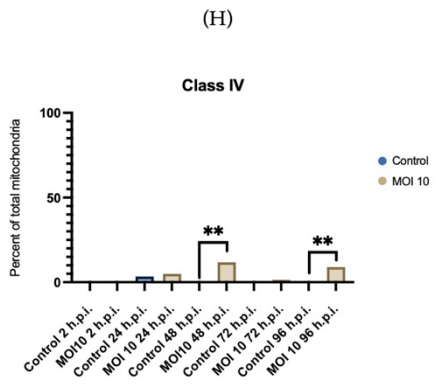
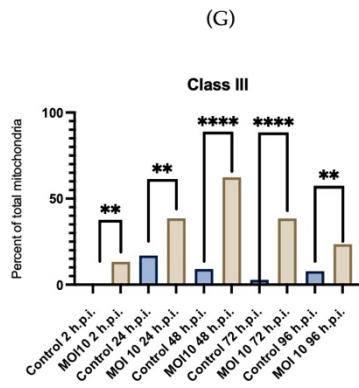
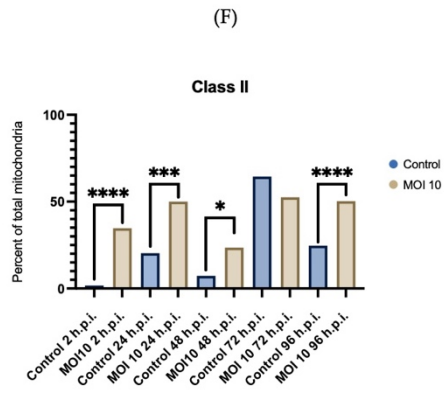
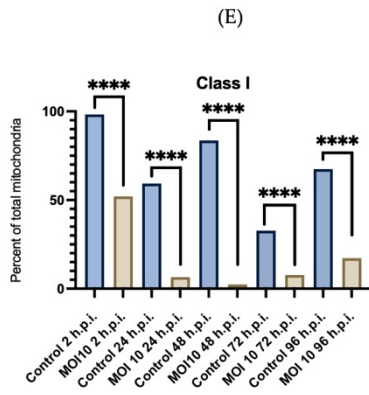
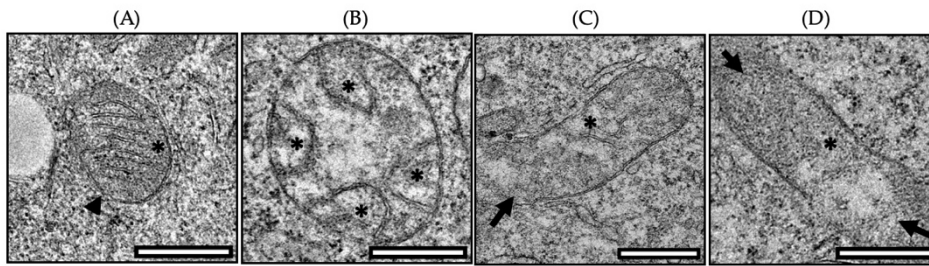


Figure 3

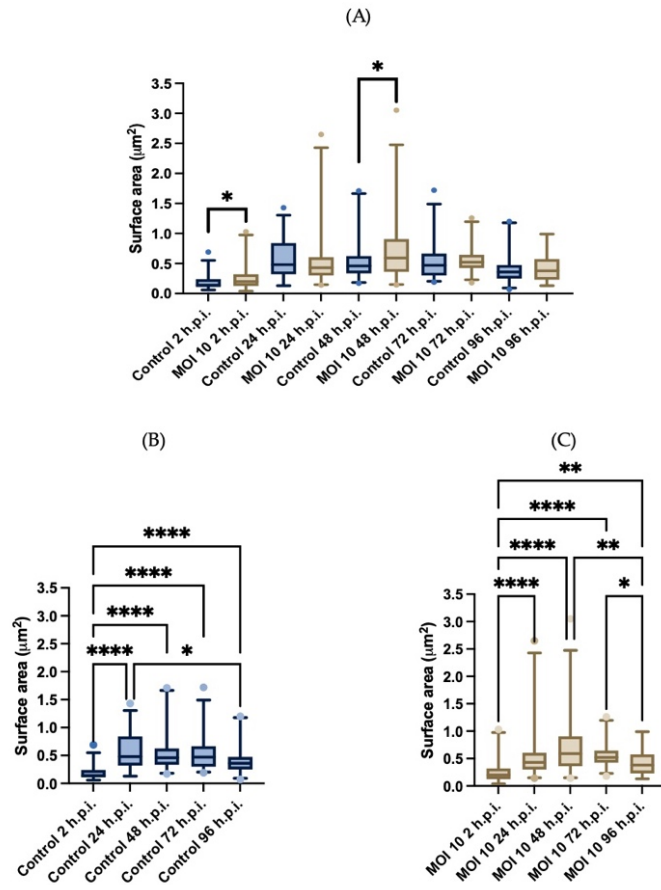


Figure 4

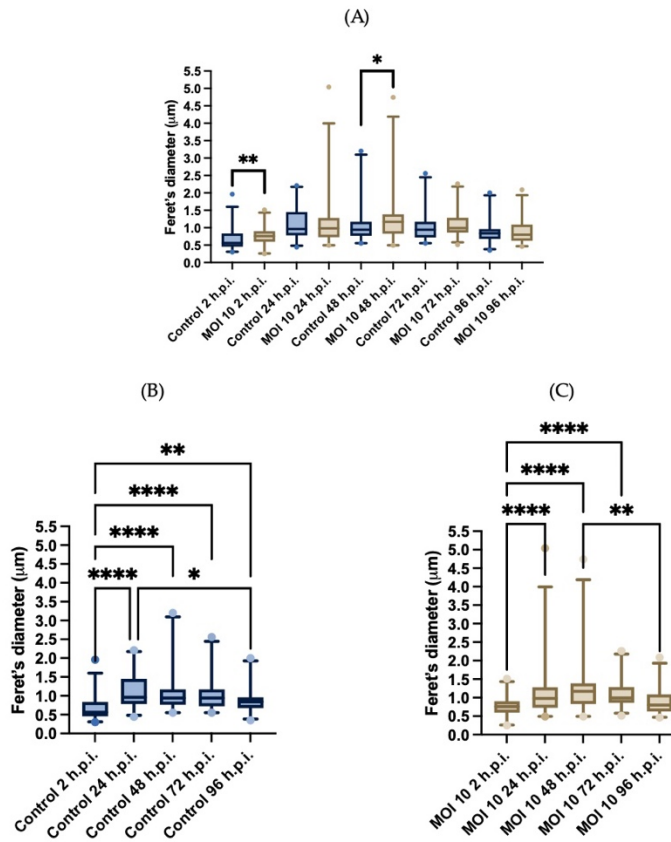


Figure 5

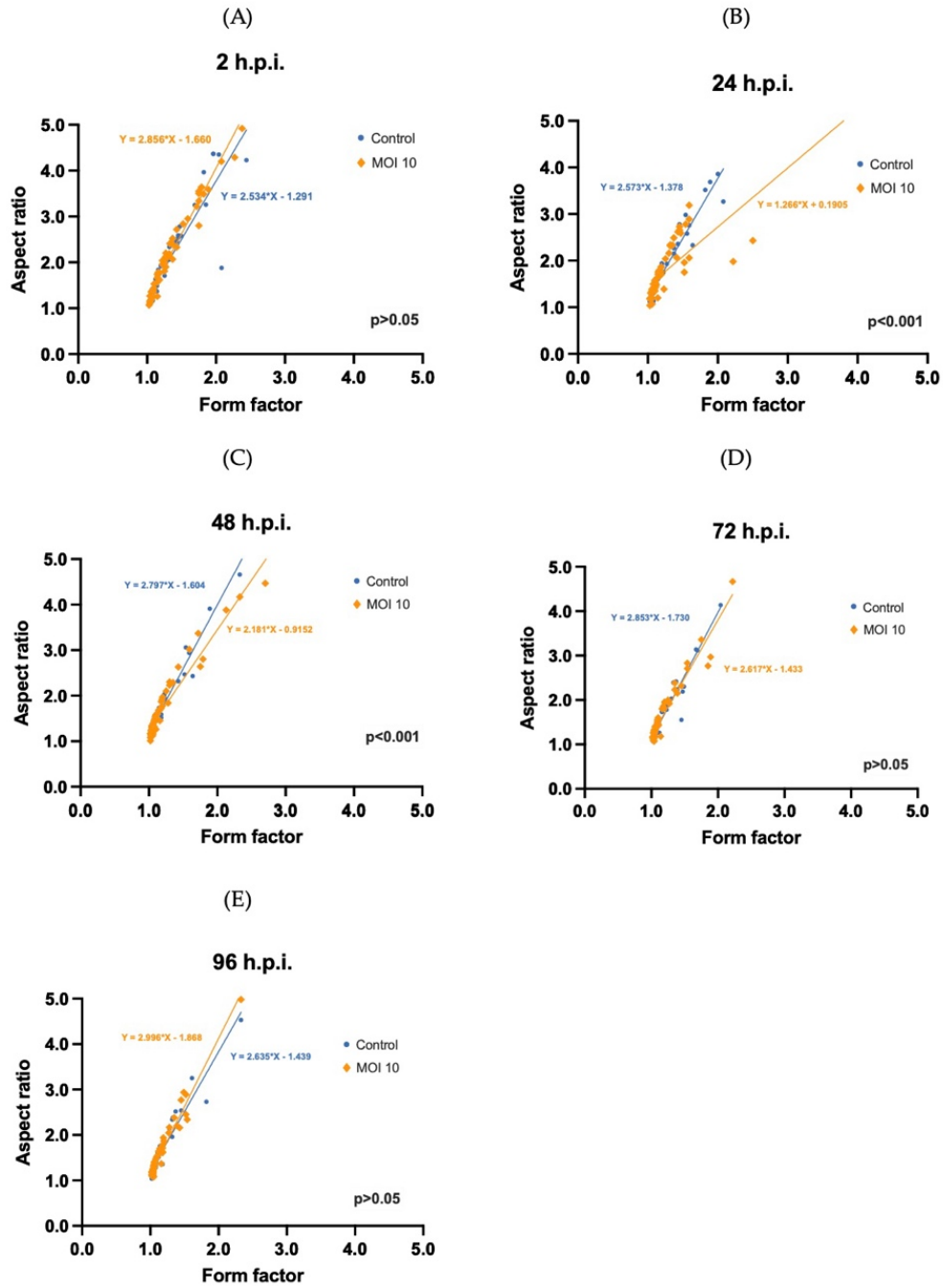


Figure 6

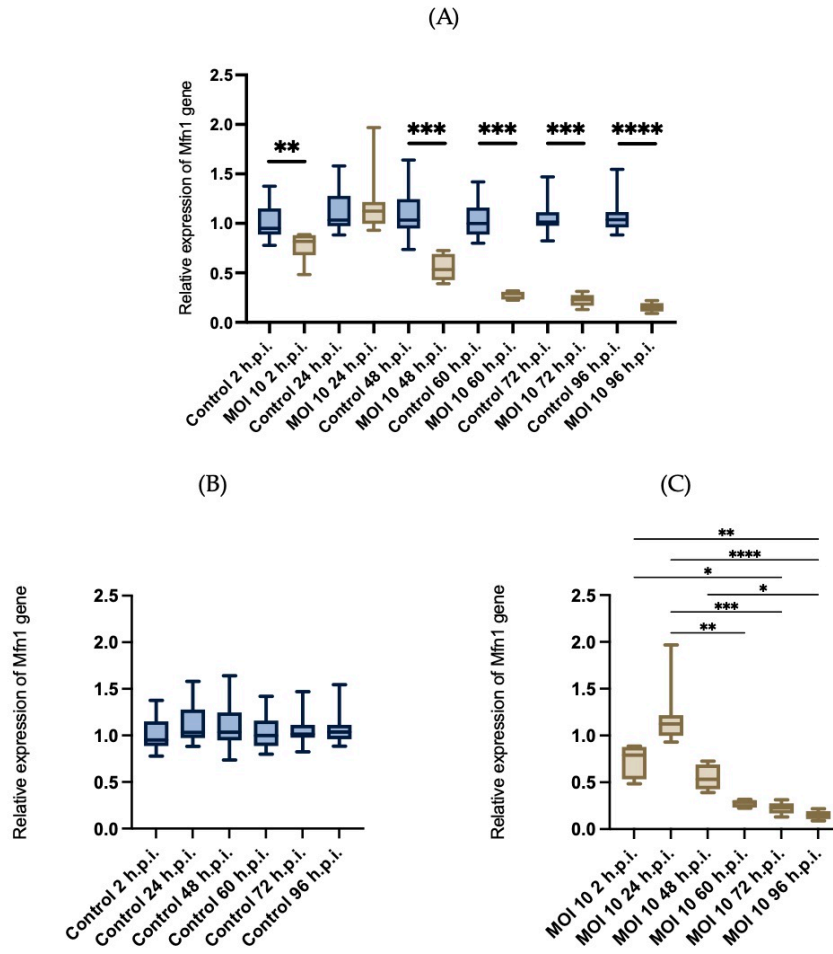


Figure 7

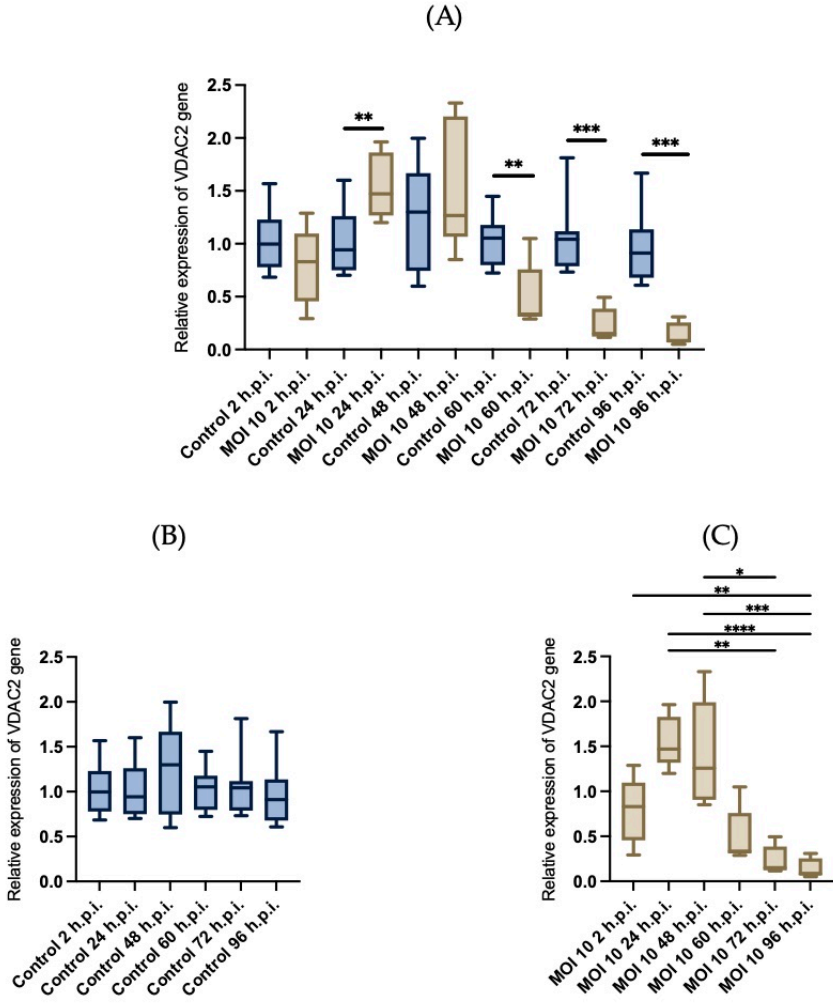


Figure 8

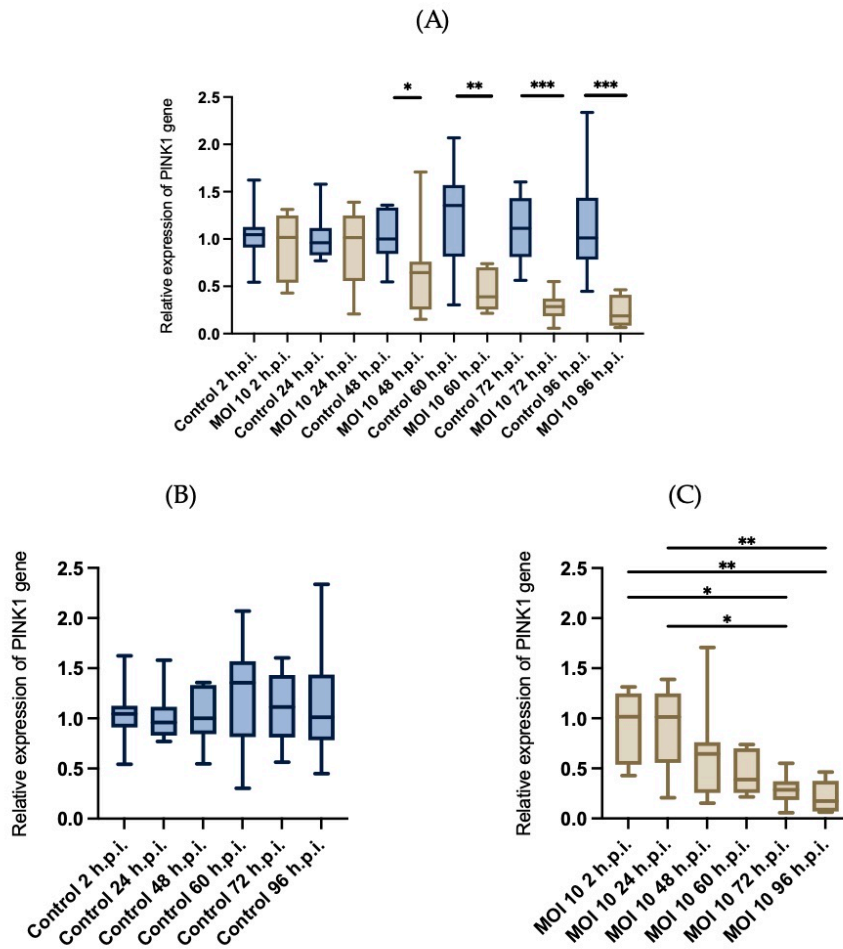


Figure S1

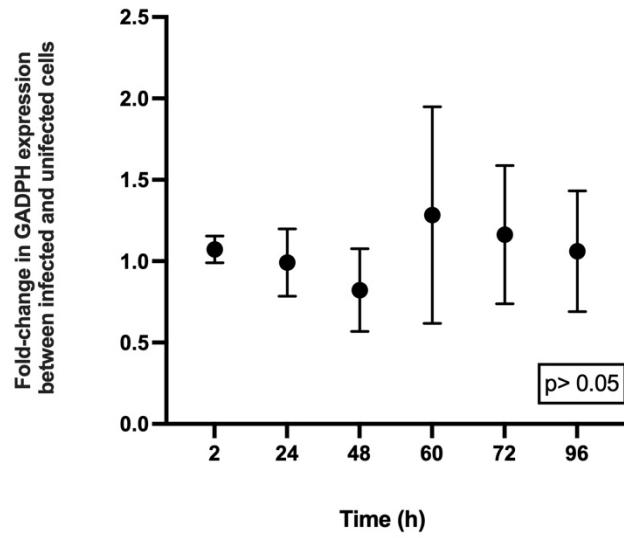
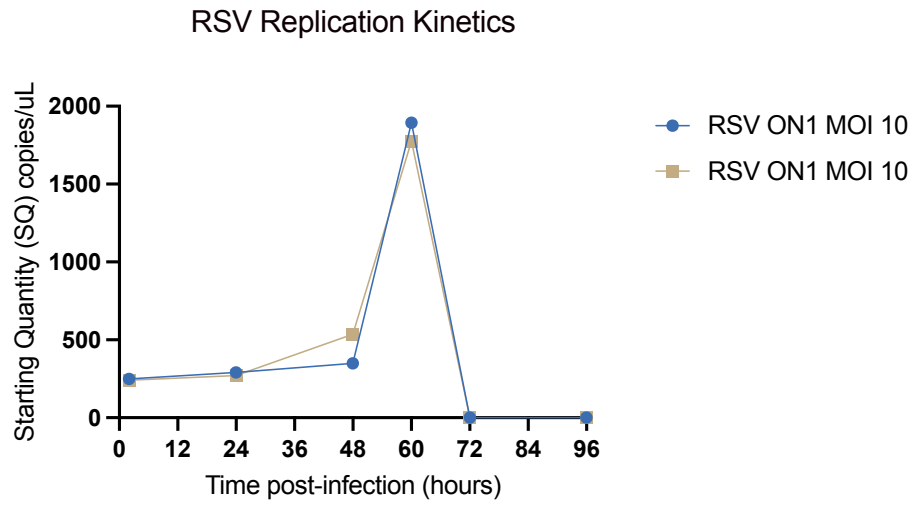


Figure S2



Publications



viruses

an Open Access Journal by MDPI



CERTIFICATE OF ACCEPTANCE



Certificate of acceptance for the manuscript (**viruses-2454150**) titled:

Ultrastructural and functional characterization of mitochondrial dynamics induced by human respiratory syncytial virus infection in HEP-2 cells.

Authored by:

Ignacio Lara-Hernandez; Juan Carlos Escalante-Muñoz; Sofia Bernal-Silva; Daniel E Noyola; Rosa Maria Wong-Chew; Andreu Comas-Garcia;
Mauricio Comas-Garcia

has been accepted in *Viruses* (ISSN 1999-4915) on 05 July 2023



Basel, July 2023

Article

Ultrastructural and Functional Characterization of Mitochondrial Dynamics Induced by Human Respiratory Syncytial Virus Infection in HEp-2 Cells

Ignacio Lara-Hernandez¹, Juan Carlos Muñoz-Escalante^{2,3} , Sofía Bernal-Silva^{3,4}, Daniel E. Noyola^{2,3} , Rosa María Wong-Chew⁵, Andreu Comas-García^{3,*}  and Mauricio Comas-García^{1,6,7,*} 

- ¹ High-Resolution Microscopy Section, Center for Research in Health Sciences and Biomedicine, Autonomous University of San Luis Potosí, San Luis Potosí 78210, Mexico; lara.ignacioh@gmail.com
 - ² Center for Research in Health Sciences and Biomedicine, Autonomous University of San Luis Potosí, San Luis Potosí 78210, Mexico; carlos.escalante@uaslp.mx (J.C.M.-E.); dnoyola@uaslp.mx (D.E.N.)
 - ³ Department of Microbiology, School of Medicine, Autonomous University of San Luis Potosí, San Luis Potosí 78210, Mexico; sofia.bernal@uaslp.mx
 - ⁴ Genomic Medicine Section, Center for Research in Health Sciences and Biomedicine, Autonomous University of San Luis Potosí, San Luis Potosí 78210, Mexico
 - ⁵ Research Division, School of Medicine, National Autonomous University of Mexico, Mexico City 04360, Mexico; rmwongch@yahoo.com.mx
 - ⁶ Science Department, Autonomous University of San Luis Potosí, San Luis Potosí 78210, Mexico
 - ⁷ Molecular and Translation Medicine Section, Center for Research in Health Sciences and Biomedicine, Autonomous University of San Luis Potosí, San Luis Potosí 78210, Mexico
- * Correspondence: andreu.comas@uaslp.mx (A.C.-G.); mauricio.comas@uaslp.mx (M.C.-G.)



Citation: Lara-Hernandez, I.; Muñoz-Escalante, J.C.; Bernal-Silva, S.; Noyola, D.E.; Wong-Chew, R.M.; Comas-García, A.; Comas-García, M. Ultrastructural and Functional Characterization of Mitochondrial Dynamics Induced by Human Respiratory Syncytial Virus Infection in HEp-2 Cells. *Viruses* **2023**, *15*, 1518. <https://doi.org/10.3390/v15071518>

Academic Editors: Mohsin Khan, Seong-Jun Kim and Aleem Siddiqui

Received: 31 May 2023

Revised: 27 June 2023

Accepted: 5 July 2023

Published: 7 July 2023



Copyright: © 2023 by the authors. Licensee MDPI, Basel, Switzerland. This article is an open access article distributed under the terms and conditions of the Creative Commons Attribution (CC BY) license (<https://creativecommons.org/licenses/by/4.0/>).

Abstract: Human respiratory syncytial virus (hRSV) is the leading cause of acute lower respiratory tract infections in children under five years of age and older adults worldwide. During hRSV infection, host cells undergo changes in endomembrane organelles, including mitochondria. This organelle is responsible for energy production in the cell and plays an important role in the antiviral response. The present study focuses on characterizing the ultrastructural and functional changes during hRSV infection using thin-section transmission electron microscopy and RT-qPCR. Here we report that hRSV infection alters mitochondrial morphodynamics by regulating the expression of key genes in the antiviral response process, such as Mfn1, VDACC2, and PINK1. Our results suggest that hRSV alters mitochondrial morphology during infection, producing a mitochondrial phenotype with shortened cristae, swollen matrix, and damaged membrane. We also observed that hRSV infection modulates the expression of the aforementioned genes, possibly as an evasion mechanism in the face of cellular antiviral response. Taken together, these results advance our knowledge of the ultrastructural alterations associated with hRSV infection and might guide future therapeutic efforts to develop effective antiviral drugs for hRSV treatment.

Keywords: human respiratory syncytial virus; mitochondrial alterations; ultrastructural characterization

1. Introduction

The human respiratory syncytial virus (hRSV), also known as human Orthopneumovirus, is an enveloped, single-stranded negative-sense RNA virus that encodes for 11 proteins. This virus belongs to the genus *Orthopneumovirus* and *Pneumoviridae* family [1]. Since it was discovered hRSV has been considered the main etiological agent of acute lower respiratory tract infections in children under the age of five and an important cause of pneumonia in elderly adults worldwide. In 2019, it was estimated that there were 33.0 million acute lower respiratory tract infections related to hRSV infections globally in children 0 to 60 months of age, of which 6.6 million were reported in infants < 6 months [2].

Chapter 1

Basic virological aspects of SARS-CoV-2

M. Comas-García^{1,2,3}, E.I. Rubio-Hernández⁴, I. Lara-Hernández², M. Colunga-Saucedo³, C.G. Castillo⁴,
A. Comas-García^{3,5}, A. Monsivais-Urenda^{6,7} and R. Zandi⁸

¹Department of Sciences, Autonomous University of San Luis Potosí, San Luis Potosí, Mexico, ²High-Resolution Microscopy Section, Research Center for Health Sciences and Biomedicine, Autonomous University of San Luis Potosí, San Luis Potosí, Mexico, ³Medical Genomics Section, CICSaB, UASLP, San Luis Potosí, Mexico, ⁴Coordination for the Innovation and Application of Science and Technology (CIACYT)—Medical School, UASLP, San Luis Potosí, Mexico, ⁵Department of Microbiology, Medical School, UASLP, San Luis Potosí, Mexico, ⁶Translational Medicine Section, CICSaB, UASLP, San Luis Potosí, Mexico, ⁷Department of Immunology, Medical School UASLP, San Luis Potosí, Mexico, ⁸Department of Physics and Astronomy, University of California, Riverside, CA, United States

1.1 Introduction

Coronaviruses (CoVs) belong to a group of positive-sense single-stranded RNA viruses that have the largest genome known for a virus and use RNA as its genetic material. These viruses can infect a wide variety of animals, causing very different diseases that include common cold (humans), peritonitis (cats), hepatitis (mouse), and life-threatening pneumonia (humans). In fact, before the year 2002, most of CoV literature focused on viruses of veterinarian interest. This changed in 2002 and 2012 with the appearance of two novel human CoVs that cause Severe Acute Respiratory Syndromes, SARS-CoV and MERS-CoV, respectively. The localized epidemics caused by these two viruses served as warning events on how zoonotic transmission of CoVs between bats (or camels) and humans could result in the formation of new viruses. Unfortunately, the research on these viruses mostly caught only the attention of the groups that either previously worked with CoVs of veterinarian interest or lived in the regions affected by SARS-CoV and MERS-CoV.

The emergence of a novel human CoV (SARS-CoV-2) in Wuhan, China at the end of 2019 changed the world. By the first trimester of 2020, this virus was almost in every continent, causing an unprecedented halt of social, academic, economic, cultural, sports, and even political activities. This pandemic not only changed the way we behave but also the way science is done. Since the release of the first full-length SARS-CoV-2 genome, in February of 2020 by the group of Prof. Zhang (Wu et al., 2020), research groups from all around the world decided to learn about CoVs and develop new research interests. Most importantly, in order to fight this pandemic, we need to develop new biomedical and biotechnological tools to understand, at least at a basic level, how CoVs (especially SARS-CoV-2) function.

The goal of this chapter is to establish the minimal virological basis required to understand the viral infectious cycle. It is not our intention to provide a detailed review of every single aspect of the viral infectious cycle but to highlight key parts of it. In fact, we apologize to everyone whose work has not been highlighted. This chapter is intended to help the reader navigate through the rest of the book and to appreciate the novel biotechnological approaches that have been developed to fight the COVID-19 pandemic. This chapter presents the different steps of the viral infectious cycle as it occurs in the cell. First, we introduce the virus by giving a description of the genome organization and the function of some of its genes; afterward, we address virion entry, replication, assembly, and egress. Finally, we added a section regarding the immune response to a viral infection. The goal of this section is to provide the readers with the minimal knowledge required to understand and appreciate the rest of the chapters.

1.2 Genome organization and function

CoVs belong to the order *Nidovirales*, family *Coronaviridae*, and subfamily *Orthocoronavirinae*, which are further divided into four genera: Alphacoronavirus, Betacoronavirus, Gammacoronavirus, and Deltacoronavirus (V'kovski et al., 2020).

Chapter 2

Fundamental aspects of the structural biology of coronaviruses

I. Lara-Hernández¹, M.A. Cornado-Ipiña¹, K. Rocha-Rosas¹ and M. Comas-García^{1,2,3}

¹High-Resolution Microscopy Section, Research Center for Health Sciences and Biomedicine, Autonomous University of San Luis Potosí, San Luis Potosí, Mexico, ²Department of Sciences, Autonomous University of San Luis Potosí, San Luis Potosí, Mexico, ³Medical Genomics Section, Research Center for Health Sciences and Biomedicine, Autonomous University of San Luis Potosí, San Luis Potosí, Mexico

2.1 Introduction

The development of structural tools to study macromolecular complexes has forever changed how we understand viruses, their interactions with the host-cell, small molecules, and antibodies (Dülfer et al., 2019; Jun et al., 2019; Koning et al., 2018; Kuhlman & Bradley, 2019; Kurta et al., 2017; Maciejewski et al., 2017; Renaud et al., 2018; Zhang, 2019). In particular, the improvements in cryo-EM made in the last decade have allowed studying viruses with atomic resolution (Strack, 2020) and publishing three-dimensional structures at a formidable rate. In fact, most of the current advances that have been accomplished since the first genome of the SARS-CoV-2 was published would be impossible without cryo-EM. Unfortunately, the structure of some viral proteins has not been solved (e.g., protein M). This can be associated to their physicochemical properties (e.g., highly hydrophobic or extremely disordered tertiary structures), which make their expression and purification extremely challenging. However, by using computational approaches, one can use a known structure of the homologous protein as template to predict the structure of a novel protein (Kuhlman & Bradley, 2019; Senior et al., 2020). Furthermore, we can use their three-dimensional structure (and/or predicted structure) to search for small molecules that could have antiviral activity (Schlicksup & Zlotnick, 2020).

The goal of this chapter is to provide some basic knowledge on the structural biology of SARS-CoV-2 that might be required in the following chapters. We have focused on the four SARS-CoV-2 structural proteins and some of the non-structural (M^{pro} and PL^{pro}) and accessory proteins (3a, 7a, 8, and 9b). We have intentionally excluded the proteins that make the replicase complex (with the exception of the two proteases) since these proteins are the focus of Chapter 4, Structural Biology of the SARS-Cov 2 Replisome: Evolutionary and Therapeutic Implications. There are some cases in which no published structures for a SARS-CoV-2 protein exist. However, we have used their sequence homology to another protein to understand possible physical properties of the protein of interest. Finally, we have also added some information regarding the role of these proteins in the viral infectious cycle and pathogenesis such that their physical and biological properties can be linked to each other and thus providing a more complete view on how SARS-CoV-2 works.

2.2 The structural proteins

2.2.1 Envelope protein

The envelope (E) protein is the smallest of the coronaviruses (CoVs) structural proteins with a molecular mass of 8 kDa (Duart et al., 2020). It is a highly hydrophobic protein; 27 of its 75 amino acids are Leu and Val, and most of these residues are located at the transmembrane (TM) domain (amino acids 12–39). The N-terminal domain (NTD) is exposed to the virion surface, while the C-terminal domain (CTD) is located inside (lumen of the organelle used for assembly) and assembles into pentameric units at the Golgi membrane (Bianchi et al., 2020). In general, the E protein participates in the assembly and egress of the viral particles (Fehr & Perlman, 2015; Surya et al., 2018). For SARS-CoV, it has been demonstrated to have an ion channel activity (Nieto-Torres et al., 2014). This activity is important for viral

Metformin inhibits Zika virus infection in trophoblast cell line

Luis Didier González-García

Instituto Nacional de Perinatología

Manuel Adrian Velazquez-Cervantes

Instituto Nacional de Perinatología

Victor Javier Cruz-Holguin

Instituto Nacional de Perinatología

Arturo Flores-Pliego

Instituto Nacional de Perinatología

Oscar Villavicencio Carrizosa

Instituto Nacional de Perinatología

Ignacio Lara-Hernandez

Universidad Autónoma de San Luis Potosí

Mauricio Comas-García

Universidad Autónoma de San Luis Potosí

Addy Cecilia Helguera-Repetto

Instituto Nacional de Perinatología

Orestes López-Ortega

Institut National de la Santé et de la Recherche Médicale (INSERM) U1151, Université Paris Descartes, Sorbonne Paris Cité

Haruki Arevalo-Romero

Institut National de la Santé et de la Recherche Médicale (INSERM) U1151, Université Paris Descartes, Sorbonne Paris Cité

Edgar Ricardo Vazquez-Martinez

Unidad de Investigación en Reproducción Humana, Instituto Nacional de Perinatología- Universidad Nacional Autónoma de México

Moises Leon Juarez (✉ moisesleoninper@gmail.com)

Instituto Nacional de Perinatología

Research Article

Keywords: metformin, AMPK, Zika virus, pregnancy, trophoblast, lipids, antiviral

Posted Date: November 7th, 2022

Thesis Defense Presentation

UNIVERSIDAD AUTÓNOMA DE SAN LUIS POTOSÍ
 FACULTAD DE MEDICINA
 CENTRO DE INVESTIGACIÓN EN CIENCIAS DE LA SALUD Y BIOMEDICINA (CICSaB)

CARACTERIZACIÓN ULTRAESTRUCTURAL DE LA INFECCIÓN *IN VITRO* DEL VIRUS SINCICIAL RESPIRATORIO

TESIS QUE PRESENTA
 M.C. IONACIO LARA HERNÁNDEZ

PARA OBTENER EL GRADO DE DOCTOR EN CIENCIAS BIOMÉDICAS BÁSICAS

COMITÉ TUTORAL
 CO-DIRECTORES DE TESIS
 DR. ANDRÉU COMAS GARCÍA
 DR. MAURICIO COMAS GARCÍA

ASESORES INTERNOS
 DRA. SOFÍA BERNAL SILVA
 DR. DANIEL ERNESTO NOYOLA CHERPITEL

ASESOR EXTERNO
 DRA. ROSA MARÍA WONG CHEW

JURADO
 PRESIDENTE DE SINODALES
 DRA. PERLA DEL CARMEN NIÑO MORENO
 SECRETARÍA DE SINODALES
 DRA. SOFÍA BERNAL SILVA
 SINODALES
 DR. DANIEL ERNESTO NOYOLA CHERPITEL
 DRA. ROSA MARÍA WONG CHEW

Virus sincicial respiratorio humano (hRSV)

Taxonomía y características

Familia: *Pneumoviridae*
 Género: *Orthopneumovirus*

Características:
 ✓ Virus envuelto
 ✓ Genoma: 15.2 kb
 ✓ ss(-)ARN

Se aisló por primera vez en 1956 de un chimpancé en cautiverio. (Morris et al., 1956)

Agente de la coriza del chimpancé (ACC)

En 1957 el virus se aisló de lactantes con enfermedad de las vías respiratorias inferiores. (Chanock et al., 1957)

Meng, Jie et al., 2020

Virus sincicial respiratorio humano (hRSV)

Clasificación

Los aislados del hRSV se clasifican en 2 grupos distintos (A y B).

VSR-A (N1-Ontario, Canadá)
 Duplicación de 72 nt, ubicada en la segunda región hipervariable del gen G.

VSR-B (BA-Buenos Aires, Argentina)
 Duplicación de 60 nt, ubicada en la segunda región hipervariable del gen G.

glicoproteína G

VSR-A: GA1-GA7, SAA1, SAA2, NA1, NA2 y **ON1**
 VSR-B: GB1-GB6, SAB1-SAB4 y BA

Comas-García et al., 2018
 Chen, J et al., 2022

Panorama epidemiológico de la infección por hRSV

A nivel mundial

Es la causa viral más importante de infección aguda del tracto respiratorio inferior en bebés y niños menores de 5 años.

2019
 33 millones de episodios de infección aguda de las vías respiratorias inferiores asociada al hRSV.

26 300 muertes por infección aguda de las vías respiratorias inferiores asociada al VSR en niños de 0 a 60 meses.

Li, You et al., 2022

Panorama epidemiológico de la infección por hRSV

En México

Casos de otros virus respiratorios (OVR) en el SISVER, México, temporada de influenza estacional 2022-2023

Se confirmaron 3 422 casos positivos a OVR

49%

Fuente: SINAVIDEGSistema de Vigilancia Epidemiológica de Enfermedad Respiratoria Viral, acceso al 04/05/2023.

Manifestaciones clínicas de la infección por hRSV

Cronología de la infección

Exposición a hRSV (día 1)

Manifestaciones clínicas de la enfermedad (días del 7 al 13)

Presentación de los primeros síntomas (días 4 a 7)

Recuperación u hospitalización (día 14)

Síntomas:

fiebre, congestión nasal, tos seca

En casos graves: respiración rápida o sibilancias, cianosis

Mayo Clinic, n.d.

Manifestaciones clínicas de la infección por hRSV

Transmisión

- **Contacto directo** (físico).
- **Contacto indirecto** (fómite), gotas (mayores a 5 µm) y aerosoles (menores a 5 µm).

Tratamiento

- No hay vacuna para el hRSV
- Palivizumab (anticuerpo monoclonal contra el epitopo A de la glucoproteína F).

Mayo Clinic, n.d.

Ciclo de replicación del hRSV

Mengjie et al., 2020

Modificaciones ultraestructurales inducidas por diversos virus

El ciclo viral infeccioso resulta en alteraciones notables de la arquitectura celular.

Las endomembranas pueden sufrir cambios drásticos debido a la estrategia de los virus para secuestrar estructuras celulares.

Romero-Grey et al., 2014

Modulación de la función mitocondrial durante la infección viral

Principales funciones

- Autofagia
- Muerte celular
- Senescencia
- Inflamación
- Homeostasis del calcio
- Respuesta inmune innata
- Producción de ATP
- Producción de ROS

Estructura

- Función: detecta si hay algún daño en la mitocondria y activar el proceso de mitofagia.

Giacomello M et al., 2020

Modulación de la función mitocondrial durante la infección viral

Dinámica mitocondrial

Respuesta antiviral

Cervantes-Silva et al., 2021

La infección por hRSV induce cambios en la abundancia y localización de proteínas mitocondriales

Investigar cambios en el proteoma de la célula huésped en respuesta a la infección por hRSV

Los cambios observados se validaron e investigaron mediante inmunofluorescencia para estudiar la localización subcelular.

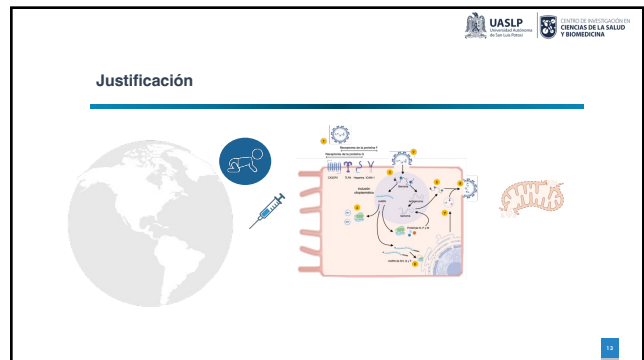
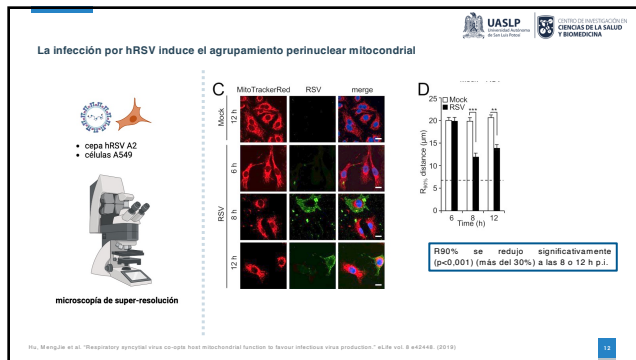
24 hp.t.

A

Mock	DAPI	VDAC1	DAPI+VDAC1
Infected	DAPI	DAPI+RSV	DAPI+VDAC1+RSV

La fluorescencia relativa de VDAC1 en las células infectadas por hRSV fue mayor que en las células control.

Munday, Diane C et al. "Quantitative proteomic analysis of A549 cells infected with human respiratory syncytial virus." Microbiol & cellular proteomics. MCP vol. 9:11 (2010)



Pregunta de investigación

¿Cuáles son las alteraciones ultraestructurales observadas en las mitocondrias de células Hep-2 infectadas con el virus sincicial respiratorio?

14

Hipótesis

Existirán cambios en la morfología de las mitocondrias, en su función y la organización de sus crestas provocadas por infección por el virus sincicial respiratorio de las células Hep-2.

15

Objetivo general

Caracterizar las alteraciones ultraestructurales en las mitocondrias de células Hep-2 inducidas por la infección del hRSV-A ON1.

16

- Objetivos específicos:
1. Determinar ultraestructuralmente las alteraciones mitocondriales de la infección *in vitro* del hRSV ON1 en células Hep-2.
 2. Analizar morfométricamente las alteraciones mitocondriales asociadas a la infección *in vitro* del hRSV ON1 en células Hep-2.
 3. Evaluar el cambio en la expresión de genes implicados en la función mitocondrial (VDAC2, Mfn1 y PINK1) durante la infección *in vitro* del hRSV ON1 en células Hep-2.
- 17

Metodología experimental

Objetivo 1 Caracterizar ultraestructuralmente las alteraciones mitocondriales de la infección in vitro del HRSV ON1 en células Hep-2

Previo a la infección Pasaje celular a placas de cultivo de 6 pozos

Se agrega tripsina y se incuba a 37°C por 5 minutos

Se neutraliza la tripsina y se agrega medio DMEM

Se disgregan las células

Se transfieren a placas de 6 pozos

Condiciones de incubación
Temperatura 37°C
CO₂: 5%

Células Hep-2 (ATCC: CCL-23)
Frasco para cultivo celular 75cm²

Lara-Hernandez et al., 2023

Metodología experimental

Objetivo 1 Caracterizar ultraestructuralmente las alteraciones mitocondriales de la infección in vitro del HRSV ON1 en células Hep-2

Cinéticas de infección

Se inoculan las muestras con HRSV ON1 a una dilución específica en PBS

Se remueve el medio de cultivo y se realizan 3 lavados con PBS 1x

Las placas se incuban durante 2 horas con agitación manual cada 15 minutos

Condiciones de incubación
Temperatura 37°C
CO₂: 5%

Lara-Hernandez et al., 2023

Metodología experimental

Objetivo 1 Caracterizar ultraestructuralmente las alteraciones mitocondriales de la infección in vitro del HRSV ON1 en células Hep-2

Cinéticas de infección

Se remueve el inóculo y se agrega medio de cultivo DMEM

Las placas se incuban durante el tiempo indicado

Condiciones de incubación
Temperatura 37°C
CO₂: 5%

	2h p.i.	24h p.i.	48h p.i.	72h p.i.	96h p.i.
MSU 10	<input checked="" type="checkbox"/>				
Control	<input checked="" type="checkbox"/>				

• Cada muestra se realizó por duplicado.

Lara-Hernandez et al., 2023

Metodología experimental

Objetivo 1 Caracterizar ultraestructuralmente las alteraciones mitocondriales de la infección in vitro del HRSV ON1 en células Hep-2

Fijación química con aldehidos

Después del periodo de incubación

Se retira el medio de las muestras
Se realizan 3 lavados con PBS 1x

Se agrega 1 mL solución fijadora

Solución fijadora
2% glutaraldehído
0.1 M cacodilato de sodio
0.2% ácido pírico

Condiciones de incubación
Temperatura ambiente durante 2 horas
Almacenar a 4°C

Lara-Hernandez et al., 2023

Metodología experimental

Objetivo 1 Caracterizar ultraestructuralmente las alteraciones mitocondriales de la infección in vitro del HRSV ON1 en células Hep-2

Post fijación química

Se remueve la solución fijadora

3 lavados con cacodilato de sodio 0.1M

Se agrega acetato de uranio al 0.5%

Se agrega tetróxido de Osmio al 1% durante 1 hora

2 lavados con cacodilato de sodio 0.1M y 1 lavado con acetato de sodio 0.1 M

3 lavados con acetato de sodio 0.1 M y 3 lavados con H₂O

Lara-Hernandez et al., 2023

Metodología experimental

Objetivo 1 Caracterizar ultraestructuralmente las alteraciones mitocondriales de la infección in vitro del HRSV ON1 en células Hep-2

Deshidratación

Se realizan lavados en serie
Con alcoholes a distintos grados (35, 50, 70, 95 y 100%)

Se retira el H₂O

Incubar por 24 hrs

Se agrega resina

- Histo-Bond
- OXON (Oxone/Ammonium Acrylate)
- Med. Quím. (Med. Quím. Análisis)
- Osm-10 (Osmium tetroxide)
- Osm-10 (Osmium tetroxide)

Inclusión y curado

Se retira la resina

3 lavados con resina

Curado de la resina

Condiciones de incubación:
Temperatura de 55 °C durante 48 horas.

Lara-Hernandez et al., 2023

Metodología experimental

Objetivo 1 Caracterizar ultraestructuralmente las alteraciones mitocondriales de la infección *in vitro* del hRSV ON1 en células Hep-2

Obtención de cortes ultrafinos

Preparación de la muestra

Ultramicrotomo Leica EM UC7
Obtención de cortes de 75 nm

Transferencia de cortes ultrafinos

Tinción por color
Azul de toluidina

Transferencia a rejillas
Rejillas de cobre de malla 100

Lara-Hernandez et al., 2023

Metodología experimental

Objetivo 1 Caracterizar ultraestructuralmente las alteraciones mitocondriales de la infección *in vitro* del hRSV ON1 en células Hep-2

Post-infección

Microscopio electrónico de transmisión

Microscopio Electrónico de Transmisión JEM-JEOL-2100 a 200 kV

Se adquirieron un total de 1200 micrografías

Lara-Hernandez et al., 2023

Metodología experimental

Objetivo 1 Caracterizar ultraestructuralmente las alteraciones mitocondriales de la infección *in vitro* del hRSV ON1 en células Hep-2

Análisis de las micrografías electrónicas

En cada muestra se evaluaron entre 50 y 150 mitocondrias.

Table 2. Qualitative scoring system [34,41]

Injury Stage	Characteristics of Mitochondria
Class I	Mitochondria are considered normal. The cristae are densely packed and longitudinal, and the matrix is electron dense.
Class II	Mitochondria in this class have rounded or asymmetrical cristae. The cristae's direction, narrowness, or regular distribution have been lost.
Class III	Mitochondria vary in size and form, with discontinuous membranes, fragmented cristae, and swollen and electron lucent matrix.
Class IV	In this class, the mitochondrial double membrane is no longer complete, and the cristae are disrupted and dispersed.

Software Fiji

Crouser E et al., 1999
Joshi M et al., 2000

Resultados

Objetivo 1 Caracterizar ultraestructuralmente las alteraciones mitocondriales de la infección *in vitro* del hRSV ON1 en células Hep-2

Micrografías representativas de la caracterización ultraestructural de las mitocondrias

2 h.p.i. 24 h.p.i. 48 h.p.i. 72 h.p.i.

Control (E, F, G, H)

hRSV (I, J, K, L)

La barra de escala corresponde a 0.5 μ m en el control y 0.75 μ m en los infectados.

Lara-Hernandez et al., 2023

Resultados

Objetivo 1 Caracterizar ultraestructuralmente las alteraciones mitocondriales de la infección *in vitro* del hRSV ON1 en células Hep-2

Micrografías representativas que ilustran la clasificación de las mitocondrias

Class II

Class IV

Figura 2. 2 x 2 (la prueba exacta de Fisher)

* correspondencia a $p < 0.05$, ** $p < 0.002$, *** $p < 0.0002$ y **** $p < 0.0001$.

Lara-Hernandez et al., 2023

Resultados

Objetivo 1 Caracterizar ultraestructuralmente las alteraciones mitocondriales de la infección *in vitro* del hRSV ON1 en células Hep-2

Nuestros hallazgos sugieren que hRSV ON1 altera la morfología mitocondrial, especialmente la forma de las membranas mitocondriales y las crestas, durante la infección.

Lara-Hernandez et al., 2023

Metodología experimental

Objetivo 2 Analizar morfométricamente las alteraciones mitocondriales asociadas a la infección in vitro del hRSV ON1 en células Hep-2

Análisis morfométrico de las micrografías electrónicas

Parámetros morfométricos

Descriptores de tamaño

- Área
- Perímetro
- Díámetro de Feret

Descriptores de forma

- Relación de aspecto
- Factor de forma

El análisis morfométrico se realizó mediante un muestreo sistemático, utilizando 25 micrografías seleccionadas al azar.

Lara-Hernández et al., 2021
Shultz Jr et al., 2019

Resultados

Objetivo 2 Analizar morfométricamente las alteraciones mitocondriales asociadas a la infección in vitro del hRSV ON1 en células Hep-2

Análisis morfométrico del área de superficie de las mitocondrias

(A) (B) (C)

U de Mano-Whitney

Lara-Hernández et al., 2023 * corresponde a $p < 0.05$, ** $p < 0.002$, *** $p < 0.0002$ y **** $p < 0.0001$

Resultados

Objetivo 2 Analizar morfométricamente las alteraciones mitocondriales asociadas a la infección in vitro del hRSV ON1 en células Hep-2

Análisis morfométrico del diámetro de Feret de las mitocondrias

(A) (B) (C)

U de Mano-Whitney

Lara-Hernández et al., 2023 * corresponde a $p < 0.05$, ** $p < 0.002$, *** $p < 0.0002$ y **** $p < 0.0001$

Resultados

Objetivo 2 Analizar morfométricamente las alteraciones mitocondriales asociadas a la infección in vitro del hRSV ON1 en células Hep-2

Análisis de la complejidad mitocondrial

2 h.p.i. 24 h.p.i. 48 h.p.i. 72 h.p.i. 96 h.p.i.

anexo 7 para determinar la similitud de las pendientes de las rectas

Lara-Hernández et al., 2023

Resultados

Objetivo 2 Analizar morfométricamente las alteraciones mitocondriales asociadas a la infección in vitro del hRSV ON1 en células Hep-2

De acuerdo a los parámetros morfométricos, nuestros resultados sugieren que hRSV ON1 induce la formación de mitocondrias hiperfusionadas en etapas tempranas.

Lara-Hernández et al., 2023

Metodología experimental

Objetivo 3 Evaluar el cambio en la expresión de genes implicados en la función mitocondrial (VDAC2, Mint1 y PINK1) durante la infección in vitro del hRSV ON1 en células Hep-2

Cinética de infección

Se remueve el medio de cultivo y se realizan 3 lavados con PBS 1X.

Se inoculan las muestras con hRSV ON1 a una dilución específica en PBS.

Las placas se incuban durante 2 horas con agitación manual cada 15 minutos.

Condiciones de incubación
Temperatura 37°C
CO₂ 5%

Lara-Hernández et al., 2023

Metodología experimental

Objetivo 3 Evaluar el cambio en la expresión de genes implicados en la función mitocondrial (VDAC2, Mfn1 y PINK1) durante la infección *in vitro* del hRSV ON1 en células Hep-2

Cinéticas de infección

Se remueve el inóculo y se agrega medio de cultivo DMEM. Las placas se incuban durante el tiempo indicado.

Condiciones de incubación: Temperatura 37°C, CO₂ 5%

	72hpi	96hpi	120hpi	144hpi	168hpi	192hpi
MDF 10	✓	✓	✓	✓	✓	✓
Control	✓	✓	✓	✓	✓	✓

Lara-Hernandez et al., 2023

Metodología experimental

Objetivo 3 Evaluar el cambio en la expresión de genes implicados en la función mitocondrial (VDAC2, Mfn1 y PINK1) durante la infección *in vitro* del hRSV ON1 en células Hep-2

Extracción de ARN

QIAamp Viral RNA Mini Kit (Qiagen)

Cuantificación de ARN

Nanodrop® Spectrophotometer ND-100

- Concentración
- Pureza

Lara-Hernandez et al., 2023

Metodología experimental

Objetivo 3 Evaluar el cambio en la expresión de genes implicados en la función mitocondrial (VDAC2, Mfn1 y PINK1) durante la infección *in vitro* del hRSV ON1 en células Hep-2

RT-PCR

Muestras de ARN de la cinética del virus

	72hpi	96hpi	120hpi	144hpi	168hpi	192hpi
MDF 10	✓	✓	✓	✓	✓	✓
Control	✓	✓	✓	✓	✓	✓

Primeros (Sequencia 5'-3')
 GAPDH-F: CAGCGCTGACAGACGGAGGC
 GAPDH-R: AGGGCGCAAGAGATGATGACG

Primeros (Sequencia 5'-3')
 PINK1-F: GAGTATGAGAGCACTACTACAG
 PINK1-R: CAGCAGTACAGAGGAGTACAG
 VDAC2-F: TGCTCTTGATATGAGGGTGG
 VDAC2-R: CCGCAAGTCTGCTGGATGG
 Mfn1-F: ACCCTTTTGTGCTAGCAAGG
 Mfn1-R: TGGACTGTGATGAGGTTGGG

- Disño: RealTime qPCR Assay Entry (Integrated DNA Technologies).
- Síntesis de los oligos: Oligo T4

Dos replicas biológicas y cada muestra se analiza por triplicado.

Lara-Hernandez et al., 2023

Metodología experimental

Objetivo 3 Evaluar el cambio en la expresión de genes implicados en la función mitocondrial (VDAC2, Mfn1 y PINK1) durante la infección *in vitro* del hRSV ON1 en células Hep-2

One Step TB Green® PrimeScript™ RT-PCR Kit II (Perfect Real Time)

Producto	Concentración inicial	Unidades	Concentración final	Unidades	Volumen final (µL de reacción)
1X One Step TB Green RT-PCR Buffer	2	x	1	x	2.0
PrimeScript 1 step Enzyme Mix 2	NA	NA	NA	NA	0.4 µL
PCR Forward & Reverse Primers	1	µM	0.2	µM	2.0
total RNA	Ver tabla de diluciones	ng/µL	10	ng/µL	2.0

Programa en termociclador:

Retranscripción	42°C	5 minutos	
	95°C	10 segundos	
Ciclado	95°C	5 segundos	40 ciclos
	60°C	20 segundos	
Curva de disociación*	60°C	95°C	0.3% incremento

Procesamiento de datos:
 • Obtención de Ct
 • Método 2^{-Ct} (ΔΔCt)

Livak K et al., 2001

Resultados

Objetivo 3 Evaluar el cambio en la expresión de genes implicados en la función mitocondrial (VDAC2, Mfn1 y PINK1) durante la infección *in vitro* del hRSV ON1 en células Hep-2

La infección por hRSV ON1 induce una regulación a la baja de la expresión de Mfn1.

U de Mann-Whitney
 * corresponde a p < 0.05, ** corresponde a p < 0.002, *** corresponde a p < 0.0002 y **** corresponde a p < 0.0001.

prueba de Friedman

Lara-Hernandez et al., 2023

Resultados

Objetivo 3 Evaluar el cambio en la expresión de genes implicados en la función mitocondrial (VDAC2, Mfn1 y PINK1) durante la infección *in vitro* del hRSV ON1 en células Hep-2

La infección por hRSV ON1 induce una regulación a la baja de la expresión de VDAC2.

U de Mann-Whitney
 * corresponde a p < 0.05, ** corresponde a p < 0.002, *** corresponde a p < 0.0002 y **** corresponde a p < 0.0001.

prueba de Friedman

Lara-Hernandez et al., 2023

Discusión

El alargamiento de las mitocondrias está mediado por la estabilización de MFN1 mediada por SIRT1

condiciones de hipoxia: CoCl₂

A

CoCl₂ - - + + +

150
75
50

Los niveles de las proteínas MFN1 y SIRT1 aumentan

Daeh, Nguyen Thi Kim et al. "Mitochondrial elongation is mediated through SIRT1-mediated MFN1 stabilization." *Cellular signaling* vol. 28 (2017): 44

La sirtuina 1 regula la función mitocondrial y la homeostasis iónica en la infección por hRSV

A **B** **C** **D** **E**

La infección por hRSV de SIRT1+ hBMSC induce una expresión significativamente mayor de HIF-1α e SIRT1

Elavasa, Srinivas et al. "Sirtuin 1 regulates mitochondrial function and ionic homeostasis in respiratory syncytial virus-infected dendritic cells." *PLoS pathogens* vol. 10 (2015): 101203

Discusión

La proteína M del hRSV puede interactuar con distintas proteínas mitocondriales

Table 1
Prediction of hRSV M interacted with the mitochondrial inner

Gene	UniProtID	Protein name	Protein domain	Function
ADP1	P08646	Adenyl Phosphotransferase 1	Adenyl Phosphotransferase	Protein tyrosine phosphatase
ADP2	G05212	Adrenomedullin	Adrenomedullin	High capacity membrane-associated cell migration
ADP3	G12124	Adrenomedullin-like protein 2	Adrenomedullin-like protein 2	ADP family receptor type 1 class B signaling
ADP4	P19188	Casprase 2	Casprase 2	Cysteine protease, MMP9 activating MMP13 and MMP14
ADP5	P19189	Casprase 3	Casprase 3	Cysteine protease, MMP9 activating MMP13 and MMP14
ADP6	P19190	Casprase 1	Casprase 1	Cysteine protease, MMP9 activating MMP13 and MMP14
ADP7	P19191	Casprase 4	Casprase 4	Cysteine protease, MMP9 activating MMP13 and MMP14
ADP8	P19192	Casprase 5	Casprase 5	Cysteine protease, MMP9 activating MMP13 and MMP14
ADP9	P19193	Casprase 6	Casprase 6	Cysteine protease, MMP9 activating MMP13 and MMP14
ADP10	P19194	Casprase 7	Casprase 7	Cysteine protease, MMP9 activating MMP13 and MMP14
ADP11	P19195	Casprase 8	Casprase 8	Cysteine protease, MMP9 activating MMP13 and MMP14
ADP12	P19196	Casprase 9	Casprase 9	Cysteine protease, MMP9 activating MMP13 and MMP14
ADP13	P19197	Casprase 10	Casprase 10	Cysteine protease, MMP9 activating MMP13 and MMP14
ADP14	P19198	Casprase 11	Casprase 11	Cysteine protease, MMP9 activating MMP13 and MMP14
ADP15	P19199	Casprase 12	Casprase 12	Cysteine protease, MMP9 activating MMP13 and MMP14
ADP16	P19200	Casprase 13	Casprase 13	Cysteine protease, MMP9 activating MMP13 and MMP14
ADP17	P19201	Casprase 14	Casprase 14	Cysteine protease, MMP9 activating MMP13 and MMP14
ADP18	P19202	Casprase 15	Casprase 15	Cysteine protease, MMP9 activating MMP13 and MMP14
ADP19	P19203	Casprase 16	Casprase 16	Cysteine protease, MMP9 activating MMP13 and MMP14
ADP20	P19204	Casprase 17	Casprase 17	Cysteine protease, MMP9 activating MMP13 and MMP14
ADP21	P19205	Casprase 18	Casprase 18	Cysteine protease, MMP9 activating MMP13 and MMP14
ADP22	P19206	Casprase 19	Casprase 19	Cysteine protease, MMP9 activating MMP13 and MMP14
ADP23	P19207	Casprase 20	Casprase 20	Cysteine protease, MMP9 activating MMP13 and MMP14
ADP24	P19208	Casprase 21	Casprase 21	Cysteine protease, MMP9 activating MMP13 and MMP14
ADP25	P19209	Casprase 22	Casprase 22	Cysteine protease, MMP9 activating MMP13 and MMP14
ADP26	P19210	Casprase 23	Casprase 23	Cysteine protease, MMP9 activating MMP13 and MMP14
ADP27	P19211	Casprase 24	Casprase 24	Cysteine protease, MMP9 activating MMP13 and MMP14
ADP28	P19212	Casprase 25	Casprase 25	Cysteine protease, MMP9 activating MMP13 and MMP14
ADP29	P19213	Casprase 26	Casprase 26	Cysteine protease, MMP9 activating MMP13 and MMP14
ADP30	P19214	Casprase 27	Casprase 27	Cysteine protease, MMP9 activating MMP13 and MMP14
ADP31	P19215	Casprase 28	Casprase 28	Cysteine protease, MMP9 activating MMP13 and MMP14
ADP32	P19216	Casprase 29	Casprase 29	Cysteine protease, MMP9 activating MMP13 and MMP14
ADP33	P19217	Casprase 30	Casprase 30	Cysteine protease, MMP9 activating MMP13 and MMP14
ADP34	P19218	Casprase 31	Casprase 31	Cysteine protease, MMP9 activating MMP13 and MMP14
ADP35	P19219	Casprase 32	Casprase 32	Cysteine protease, MMP9 activating MMP13 and MMP14
ADP36	P19220	Casprase 33	Casprase 33	Cysteine protease, MMP9 activating MMP13 and MMP14
ADP37	P19221	Casprase 34	Casprase 34	Cysteine protease, MMP9 activating MMP13 and MMP14
ADP38	P19222	Casprase 35	Casprase 35	Cysteine protease, MMP9 activating MMP13 and MMP14
ADP39	P19223	Casprase 36	Casprase 36	Cysteine protease, MMP9 activating MMP13 and MMP14
ADP40	P19224	Casprase 37	Casprase 37	Cysteine protease, MMP9 activating MMP13 and MMP14
ADP41	P19225	Casprase 38	Casprase 38	Cysteine protease, MMP9 activating MMP13 and MMP14
ADP42	P19226	Casprase 39	Casprase 39	Cysteine protease, MMP9 activating MMP13 and MMP14
ADP43	P19227	Casprase 40	Casprase 40	Cysteine protease, MMP9 activating MMP13 and MMP14
ADP44	P19228	Casprase 41	Casprase 41	Cysteine protease, MMP9 activating MMP13 and MMP14
ADP45	P19229	Casprase 42	Casprase 42	Cysteine protease, MMP9 activating MMP13 and MMP14
ADP46	P19230	Casprase 43	Casprase 43	Cysteine protease, MMP9 activating MMP13 and MMP14
ADP47	P19231	Casprase 44	Casprase 44	Cysteine protease, MMP9 activating MMP13 and MMP14
ADP48	P19232	Casprase 45	Casprase 45	Cysteine protease, MMP9 activating MMP13 and MMP14
ADP49	P19233	Casprase 46	Casprase 46	Cysteine protease, MMP9 activating MMP13 and MMP14
ADP50	P19234	Casprase 47	Casprase 47	Cysteine protease, MMP9 activating MMP13 and MMP14
ADP51	P19235	Casprase 48	Casprase 48	Cysteine protease, MMP9 activating MMP13 and MMP14
ADP52	P19236	Casprase 49	Casprase 49	Cysteine protease, MMP9 activating MMP13 and MMP14
ADP53	P19237	Casprase 50	Casprase 50	Cysteine protease, MMP9 activating MMP13 and MMP14
ADP54	P19238	Casprase 51	Casprase 51	Cysteine protease, MMP9 activating MMP13 and MMP14
ADP55	P19239	Casprase 52	Casprase 52	Cysteine protease, MMP9 activating MMP13 and MMP14
ADP56	P19240	Casprase 53	Casprase 53	Cysteine protease, MMP9 activating MMP13 and MMP14
ADP57	P19241	Casprase 54	Casprase 54	Cysteine protease, MMP9 activating MMP13 and MMP14
ADP58	P19242	Casprase 55	Casprase 55	Cysteine protease, MMP9 activating MMP13 and MMP14
ADP59	P19243	Casprase 56	Casprase 56	Cysteine protease, MMP9 activating MMP13 and MMP14
ADP60	P19244	Casprase 57	Casprase 57	Cysteine protease, MMP9 activating MMP13 and MMP14
ADP61	P19245	Casprase 58	Casprase 58	Cysteine protease, MMP9 activating MMP13 and MMP14
ADP62	P19246	Casprase 59	Casprase 59	Cysteine protease, MMP9 activating MMP13 and MMP14
ADP63	P19247	Casprase 60	Casprase 60	Cysteine protease, MMP9 activating MMP13 and MMP14
ADP64	P19248	Casprase 61	Casprase 61	Cysteine protease, MMP9 activating MMP13 and MMP14
ADP65	P19249	Casprase 62	Casprase 62	Cysteine protease, MMP9 activating MMP13 and MMP14
ADP66	P19250	Casprase 63	Casprase 63	Cysteine protease, MMP9 activating MMP13 and MMP14
ADP67	P19251	Casprase 64	Casprase 64	Cysteine protease, MMP9 activating MMP13 and MMP14
ADP68	P19252	Casprase 65	Casprase 65	Cysteine protease, MMP9 activating MMP13 and MMP14
ADP69	P19253	Casprase 66	Casprase 66	Cysteine protease, MMP9 activating MMP13 and MMP14
ADP70	P19254	Casprase 67	Casprase 67	Cysteine protease, MMP9 activating MMP13 and MMP14
ADP71	P19255	Casprase 68	Casprase 68	Cysteine protease, MMP9 activating MMP13 and MMP14
ADP72	P19256	Casprase 69	Casprase 69	Cysteine protease, MMP9 activating MMP13 and MMP14
ADP73	P19257	Casprase 70	Casprase 70	Cysteine protease, MMP9 activating MMP13 and MMP14
ADP74	P19258	Casprase 71	Casprase 71	Cysteine protease, MMP9 activating MMP13 and MMP14
ADP75	P19259	Casprase 72	Casprase 72	Cysteine protease, MMP9 activating MMP13 and MMP14
ADP76	P19260	Casprase 73	Casprase 73	Cysteine protease, MMP9 activating MMP13 and MMP14
ADP77	P19261	Casprase 74	Casprase 74	Cysteine protease, MMP9 activating MMP13 and MMP14
ADP78	P19262	Casprase 75	Casprase 75	Cysteine protease, MMP9 activating MMP13 and MMP14
ADP79	P19263	Casprase 76	Casprase 76	Cysteine protease, MMP9 activating MMP13 and MMP14
ADP80	P19264	Casprase 77	Casprase 77	Cysteine protease, MMP9 activating MMP13 and MMP14
ADP81	P19265	Casprase 78	Casprase 78	Cysteine protease, MMP9 activating MMP13 and MMP14
ADP82	P19266	Casprase 79	Casprase 79	Cysteine protease, MMP9 activating MMP13 and MMP14
ADP83	P19267	Casprase 80	Casprase 80	Cysteine protease, MMP9 activating MMP13 and MMP14
ADP84	P19268	Casprase 81	Casprase 81	Cysteine protease, MMP9 activating MMP13 and MMP14
ADP85	P19269	Casprase 82	Casprase 82	Cysteine protease, MMP9 activating MMP13 and MMP14
ADP86	P19270	Casprase 83	Casprase 83	Cysteine protease, MMP9 activating MMP13 and MMP14
ADP87	P19271	Casprase 84	Casprase 84	Cysteine protease, MMP9 activating MMP13 and MMP14
ADP88	P19272	Casprase 85	Casprase 85	Cysteine protease, MMP9 activating MMP13 and MMP14
ADP89	P19273	Casprase 86	Casprase 86	Cysteine protease, MMP9 activating MMP13 and MMP14
ADP90	P19274	Casprase 87	Casprase 87	Cysteine protease, MMP9 activating MMP13 and MMP14
ADP91	P19275	Casprase 88	Casprase 88	Cysteine protease, MMP9 activating MMP13 and MMP14
ADP92	P19276	Casprase 89	Casprase 89	Cysteine protease, MMP9 activating MMP13 and MMP14
ADP93	P19277	Casprase 90	Casprase 90	Cysteine protease, MMP9 activating MMP13 and MMP14
ADP94	P19278	Casprase 91	Casprase 91	Cysteine protease, MMP9 activating MMP13 and MMP14
ADP95	P19279	Casprase 92	Casprase 92	Cysteine protease, MMP9 activating MMP13 and MMP14
ADP96	P19280	Casprase 93	Casprase 93	Cysteine protease, MMP9 activating MMP13 and MMP14
ADP97	P19281	Casprase 94	Casprase 94	Cysteine protease, MMP9 activating MMP13 and MMP14
ADP98	P19282	Casprase 95	Casprase 95	Cysteine protease, MMP9 activating MMP13 and MMP14
ADP99	P19283	Casprase 96	Casprase 96	Cysteine protease, MMP9 activating MMP13 and MMP14
ADP100	P19284	Casprase 97	Casprase 97	Cysteine protease, MMP9 activating MMP13 and MMP14
ADP101	P19285	Casprase 98	Casprase 98	Cysteine protease, MMP9 activating MMP13 and MMP14
ADP102	P19286	Casprase 99	Casprase 99	Cysteine protease, MMP9 activating MMP13 and MMP14
ADP103	P19287	Casprase 100	Casprase 100	Cysteine protease, MMP9 activating MMP13 and MMP14

Kapoor, Sarit et al. "New host factors important for respiratory syncytial virus (RSV) replication revealed by a novel microfluidic screen for interactions of matrix (M) protein." *Molecular & cellular proteomics* vol. 14(3) (2015): 49

Discusión

VDAC2 induce apoptosis en la infección por el virus de la enfermedad de bursitis

J

Survival cells

Percentage

Normal cells
Con-RNAi
VDAC2-RNAi

Normal cells
Con-RNAi
VDAC2-RNAi

Mock IBDV infection

El siRNA contra VDAC2 mostró niveles significativamente más bajos de apoptosis inducida por IBDV

Li, Zhonghua et al. "Critical role for voltage-dependent anion channel 2 in infectious bursitis disease virus-induced apoptosis in host cells via interaction with VPS." *Journal of virology* vol. 84 (2) (2012): 50

Discusión

La infección viral regula a la baja la expresión de PINK1

A

PINK1 mRNA

0 6 12 24(h)

PMs

□ VSV
■ RSV
■ HSV

Zhou, Jun et al. "Mitochondrial Protein PINK1 Positively Regulates RLR Signaling." *Frontiers in immunology* vol. 10 (2019): 51

Conclusiones

Estudios previos

morfología

- mitocondrias hinchadas
- mitocondrias elongadas

función

- alteraciones específicas de proteínas

Nuestros hallazgos

morfología

- Calitativa: nivel de daño mitocondrial
- Cuantitativa: alteración de la forma y el tamaño de la mitocondria

función

- modulación de genes implicados en la respuesta inmune, apoptosis y mitofagia

Mfn1 VDAC2 PINK1

52

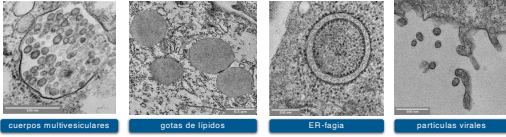
Conclusiones

El virus sincicial respiratorio inhibe la expresión de genes relacionados a vías de señalización de la respuesta inmune, apoptosis y mitofagia. Con la finalidad de propagarse mediante el contacto célula a célula.

53

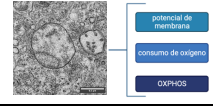
Perspectivas

- Caracterizar las modificaciones ultraestructurales observadas en otros organelos



cuerpos multivesiculares gotas de lípidos ER-fagia partículas virales

- Evaluar el daño en la función mitocondrial inducido por la infección por hRSV ON1

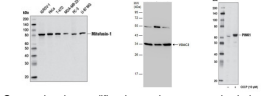


potencial de membrana
consumo de oxígeno
OXPHOS

54

Perspectivas

- Realizar Western Blot de las proteínas Mfn1, VDAC2, PINK1

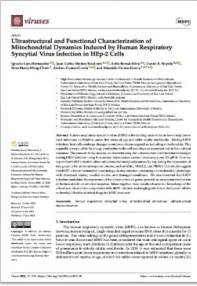


- Caracterizar las modificaciones ultraestructurales inducidas por otra variante (NA1)



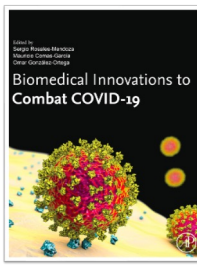
55

Publicaciones



56

Publicaciones



Chapter 1
Basic virological aspects of SARS-CoV-2

Chapter 2
Fundamental aspects of the structural biology of coronaviruses

57

Publicaciones en preprint



Metformin inhibits Zika virus infection in trophoblast cell line

58

Actividades de divulgación



ALTERNANCIA JUVENIL POR MÉXICO - SAN LUIS POTOSÍ

M.C. Ignacio Lara Hernández



Reconocimiento

M.C. Ignacio Lara Hernández



CONSTANCIA

M.C. Ignacio Lara Hernández

59

Actividades de docencia

14

Otras actividades

- Muestras biológicas para investigación académica.
- Muestras biológicas para diagnóstico médico.

Muestras registradas: 98
Muestras procesadas y cortadas en total: 537

Técnicos:

- Dr. Alejandro Ibañez Salazar (2019)
- Ing. Karina Rocha Rosas (2019-2020)
- Biol. Miguel Angel Coronado Ipiña (2021-2022)

15

Colaboraciones

16

Agradecimientos

- CONACYT por la beca otorgada con número (CVU) 775699
- Dr. Mauricio Comas García
- Dr. Andreu Comas García
- Dra. Sofía Bernal Silva
- Dr. Daniel Ernesto Noyola Cherpitel
- Dra. Rosa María Wong Chew
- Dr. Juan Carlos Muñoz Escalante
- Departamento de Microbiología de la Facultad de Medicina
- Sección de Microscopía de Alta Resolución del Centro de Investigación en Ciencias de la Salud y Biomedicina (CICSaB)

15

¡Muchas gracias por su atención!

14